Lappeenranta
University of Technology

Vesa Ruuskanen

DESIGN ASPECTS OF MEGAWATT-RANGE DIRECT-DRIVEN PERMANENT MAGNET WIND GENERATORS

Thesis for the degree of Doctor of Science (Technology) to be presented with due permission for public examination and criticism in the Auditorium 1382 at Lappeenranta University of Technology, Lappeenranta, Finland on the 22nd of December, 2011, at noon.

Acta Universitatis
Lappeenrantaensis 458

Supervisors

Professor Juha Pyrhönen
Department of Electrical Engineering
Lappeenranta University of Technology
Finland

D.Sc. Janne Nerg
Department of Electrical Engineering
Lappeenranta University of Technology
Finland

Reviewers and opponents

Emeritus Professor Tim Miller
Department of Electronics and Electrical Engineering
University of Glasgow
United Kingdom

Professor Henk Polinder
Department of Electrical Sustainable Energy
Delft University of Technology
the Netherlands

ISBN 978-952-265-183-9
ISBN 978-952-265-184-6 (PDF)
ISSN 1456-4491

Lappeenrannan teknillinen yliopisto
Digipaino 2011

Abstract

Lappeenranta University of Technology
Acta Universitatis Lappeenrantaensis 458

Vesa Ruuskanen

Design Aspects of Megawatt-Range Direct-Driven Permanent Magnet Wind Generators

Lappeenranta 2011

ISBN 978-952-265-183-9
ISBN 978-952-265-184-6 (PDF)
ISSN 1456-4491

Direct-driven permanent magnet synchronous generator is one of the most promising topologies for megawatt-range wind power applications. The rotational speed of the direct-driven generator is very low compared with the traditional electrical machines. The low rotational speed requires high torque to produce megawatt-range power. The special features of the direct-driven generators caused by the low speed and high torque are discussed in this doctoral thesis. Low speed and high torque set high demands on the torque quality. The cogging torque and the load torque ripple must be as low as possible to prevent mechanical failures. In this doctoral thesis, various methods to improve the torque quality are compared with each other. The rotor surface shaping, magnet skew, magnet shaping, and the asymmetrical placement of magnets and stator slots are studied not only by means of torque quality, but also the effects on the electromagnetic performance and manufacturability of the machine are discussed.

The heat transfer of the direct-driven generator must be designed to handle the copper losses of the stator winding carrying high current density and to keep the temperature of the magnets low enough. The cooling system of the direct-driven generator applying the doubly radial air cooling with numerous radial cooling ducts was modeled with a lumped-parameter-based thermal network. The performance of the cooling system was discussed during the steady and transient states. The effect of the number and width of radial cooling ducts was explored.

The large number of radial cooling ducts drastically increases the impact of the stack end area effects, because the stator stack consists of numerous substacks. The effects of the radial cooling ducts on the effective axial length of the machine were studied by analyzing the cross-section of the machine in the axial direction. The method to compensate the magnet end area leakage was considered. The effect of the cooling ducts and the stack end area effects on the

no-load voltages and inductances of the machine were explored by using numerical analysis tools based on the three-dimensional finite element method.

The electrical efficiency of the permanent magnet machine with different control methods was estimated analytically over the whole speed and torque range. The electrical efficiencies achieved with the most common control methods were compared with each other. The stator voltage increase caused by the armature reaction was analyzed. The effect of inductance saturation as a function of load current was implemented to the analytical efficiency calculation.

Keywords: Permanent magnet synchronous generator, direct-driven, torque quality, end effects, thermal analysis
UDC 621.548:621.311.245:537.612

Acknowledgments

The research documented in this doctoral dissertation was carried out at the Institute of Energy Technology (LUT Energy) at Lappeenranta University of Technology (LUT) during the years 2008–2011. The research was funded by the Graduate School of Electrical Energy Engineering (GSEEE), the Academy of Finland, and The Switch Engineering Oy.

The financial support by Walter Ahlström Foundation, Aimo Puromäki Foundation by the Economic Sciences and Technology Foundation KAUTE, Fortum Foundation, Ulla Tuominen Foundation, and The Finnish Cultural Foundation, The South Karelia Regional Fund is highly appreciated. In particular, the continual support from Walter Ahlström Foundation has been very profitable for the research reported in this thesis.

I would like to thank Professor Juha Pyrhönen for giving me an opportunity to participate in this research project. Dr. Janne Nerg deserves my sincerest thanks for his guidance, encouragement, and excellent advice during the process. Dr. Markku Niemelä is thanked for his valuable comments on my thesis and providing the measurement results to verify the no-load voltage of the 3D FEM model.

The comments by the preliminary examiners, Emeritus Professor Tim Miller and Professor Henk Polinder, are highly appreciated. I am especially grateful that they were able to carry out the review process in such a short time frame.

I would like to express my gratitude to Dr. Hanna Niemelä for her never-ending work to improve the language of my thesis and articles.

The co-operation with the staff of The Switch has opened many new opportunities for the research reported in this thesis, along with setting the guidelines of the project. The mechanical engineers from LUT Metal Technology with Dr. Jussi Sopanen from the Saimaa University of Applied Sciences have set important boundary conditions for the electrical engineers to design electromagnetic circuits that they can process into generators that keep running for decades. I would also thank my colleagues Mr Henry Hämäläinen and Ms Paula Immonen for the many new ideas that have arisen in our conversations.

Finally, I express my gratitude to my family. I thank my wife Susanna for her encouragement

and patience over the years. Last but not least, I express my gratitude to my parents in Finnish: "Kiitän teitä äitini Terttu ja isäni Paavo kaikesta siitä tuesta ja kannustuksesta, jota olen teiltä elämäni aikana saanut."

Lappeenranta, November 30th, 2011

Vesa Ruuskanen

Contents

List of Symbols and Abbreviations

Roman Letters

A	area of the rotor of the turbine $\left[\mathrm{m}^2\right]$, linear current density $\left[\frac{\mathrm{A}}{\mathrm{m}}\right]$
a	order of harmonic component [-]
B	flux density $\left[\frac{\mathrm{Vs}}{\mathrm{m}^2}\right]$
B_{homog}	flux density of the homogeneous infinitely long machine $\left[\frac{\mathrm{Vs}}{\mathrm{m}^2}\right]$
B_{n}	flux density normal component $\left[\frac{\mathrm{Vs}}{\mathrm{m}^2}\right]$
B_{r}	remanent flux density $\left[\frac{\mathrm{Vs}}{\mathrm{m}^2}\right]$
$\vec{B}_{\mathrm{r}}$	rotor flux density vector $\left[\frac{\mathrm{Vs}}{\mathrm{m}^2}\right]$
$\vec{B}_{\mathrm{s}}$	stator flux density vector $\left[\frac{\mathrm{Vs}}{\mathrm{m}^2}\right]$
b	order of harmonic component [-], cooling duct width $[\mathrm{m}]$
$\mathbf{C}$	thermal capacitance matrix $\left[\frac{\mathrm{Vs}}{\mathrm{m}^2}\right]$
C_{p}	power coefficient [-]
$C_{\mathrm{th},i}$	thermal capacitance of the element i $\left[\frac{\mathrm{J}}{\mathrm{K}}\right]$
c_{p}	heat capacity of the fluid $\left[\frac{\mathrm{J}}{\mathrm{kgK}}\right]$
E_{PM}	no-load phase voltage RMS value $[\mathrm{V}]$
$E_{\mathrm{PM},x\ \mathrm{mm}}$	no-load voltage with the physical stack length x $[\mathrm{V}]$
$\vec{e}_{\mathrm{PM}}$	no-load voltage vector $[\mathrm{V}]$
$\vec{e}_{\mathrm{s}}$	stator back electromotive force vector $[\mathrm{V}]$
f	frequency $[\mathrm{Hz}]$
f_{n}	nominal frequency $[\mathrm{Hz}]$
$\mathbf{G}$	thermal conductance matrix $\left[\frac{\mathrm{W}}{\mathrm{K}}\right]$

$\mathbf{G}_{\mathrm{fluid}}$	cooling matrix $\left[\frac{\mathrm{W}}{\mathrm{K}}\right]$
H_{n}	magnetic field strength normal component $\left[\frac{\mathrm{A}}{\mathrm{m}}\right]$
H_{tan}	magnetic field strength tangential component $\left[\frac{\mathrm{A}}{\mathrm{m}}\right]$
h_{PM}	height of the permanent magnet $[\mathrm{m}]$
i	number of node of the thermal resistance network [-]
i_{b}	current base value $[\mathrm{A}]$
i_{d}	direct-axis current $[\mathrm{A}]$
$i_{\mathrm{d,n}}$	direct-axis current normalized value $[\mathrm{A}]$
$i_{\mathrm{d,nref}}$	reference value for the direct-axis normalized current $[\mathrm{A}]$
i_{q}	quadrature-axis current $[\mathrm{A}]$
$i_{\mathrm{q,n}}$	quadrature-axis current normalized value $[\mathrm{A}]$
$i_{\mathrm{q,nref}}$	reference value for the quadrature-axis normalized current $[\mathrm{A}]$
$\vec{i}_{\mathrm{s}}$	stator current vector $[\mathrm{A}]$
i_{sd}	direct-axis current component of one coil turn $[\mathrm{A}]$
i_{sq}	quadrature-axis current component of one coil turn $[\mathrm{A}]$
j	number of node of the thermal resistance network [-], index implementing different materials [-]
j	imaginary unit
$\vec{\mathrm{j}}$	imaginary vector, $\vec{\mathrm{j}} = 0 + 1\mathrm{j}$
k	order of harmonic [-]
k_{f}	space factor of the lamination core [-]
L	inductance $\left[\frac{\mathrm{Vs}}{\mathrm{A}}\right]$
L_{d}	direct-axis synchronous inductance $\left[\frac{\mathrm{Vs}}{\mathrm{A}}\right]$
L_{m}	magnetization inductance $\left[\frac{\mathrm{Vs}}{\mathrm{A}}\right]$
L_{md}	direct-axis magnetization inductance $\left[\frac{\mathrm{Vs}}{\mathrm{A}}\right]$
L_{mq}	quadrature-axis magnetization inductance $\left[\frac{\mathrm{Vs}}{\mathrm{A}}\right]$
L_{q}	quadrature-axis synchronous inductance $\left[\frac{\mathrm{Vs}}{\mathrm{A}}\right]$
L_{s}	stator total inductance $\left[\frac{\mathrm{Vs}}{\mathrm{A}}\right]$
L_{σ}	stator stray inductance $\left[\frac{\mathrm{Vs}}{\mathrm{A}}\right]$

l	physical length of the machine $[\mathrm{m}]$
l'	effective length of the machine $[\mathrm{m}]$
$l_{x\ \mathrm{mm}}$	physical length x of the stack $[\mathrm{m}]$
l_{ends}	sum of the effective length of the end regions $[\mathrm{m}]$
m	mass $[\mathrm{kg}]$
N_{ph}	number of series-connected coil turns [-]
n	number of nodes of the thermal resistance network [-], number of radial cooling ducts [-]
$\mathbf{P}$	loss vector $[\mathrm{W}]$
P_{t}	power of the turbine $[\mathrm{W}]$
P_{w}	power of the wind $[\mathrm{W}]$
p	number of pole pairs [-]
q	number of slots per pole and phase [-]
q_{v}	volume flow rate $\left[\frac{\mathrm{m}^3}{\mathrm{s}}\right]$
R_{q}	thermal resistance for the cooling matrix $\left[\frac{\mathrm{K}}{\mathrm{W}}\right]$
$R_{\mathrm{q}ii}$	thermal resistance of the cooling fluid passing the node i $\left[\frac{\mathrm{K}}{\mathrm{W}}\right]$
$R_{\mathrm{q}ij}$	thermal resistance of the cooling fluid between nodes i and j $\left[\frac{\mathrm{K}}{\mathrm{W}}\right]$
R_{s}	stator resistance $\left[\frac{\mathrm{V}}{\mathrm{A}}\right]$
$R_{x,y}$	thermal resistance between nodes x and y $\left[\frac{\mathrm{K}}{\mathrm{W}}\right]$
r_k	amplitude of the k^{th} rotor harmonic $\left[\frac{\mathrm{Vs}}{\mathrm{m}^2}\right]$
s_k	amplitude of the k^{th} stator harmonic $\left[\frac{\mathrm{Vs}}{\mathrm{m}^2}\right]$
T	torque $[\mathrm{Nm}]$
$\mathbf{T}$	temperature matrix $[\mathrm{K}]$
T_{b}	torque base value $[\mathrm{Nm}]$
T_{n}	torque normalized value [-]
T_{nref}	reference value for the normalized torque [-]
t	time $[\mathrm{s}]$
U_{s}	stator phase voltage RMS value $[\mathrm{V}]$
$U_{\mathrm{s,n}}$	nominal stator phase voltage RMS value $[\mathrm{V}]$
u_{d}	direct-axis voltage component $[\mathrm{V}]$

u_q	quadrature-axis voltage component $[\mathrm{V}]$
$\vec{u}_\mathrm{s}$	stator phase voltage vector $[\mathrm{V}]$
v_w	wind speed $\left[\frac{\mathrm{m}}{\mathrm{s}}\right]$
x	sum of harmonic components [-]
z	coordinate in the axial direction [-]

Greek Letters

δ	load angle $[\mathrm{rad}]$, length of the physical air gap $[\mathrm{m}]$
Θ	current linkage $[\mathrm{A}]$
Θ_sd	stator direct-axis current linkage $[\mathrm{A}]$
Θ_sq	stator quadrature-axis current linkage $[\mathrm{A}]$
θ	angle along the air gap $[\mathrm{rad}]$
κ	factor defined by the machine geometry [-]
μ_0	vacuum permeability $\left[\frac{\mathrm{Vs}}{\mathrm{Am}}\right]$, $\mu_0 \approx 4\pi \cdot 10^{-7}\ \frac{\mathrm{Vs}}{\mathrm{Am}}$
μ_r	relative permeability [-]
$\mu_\mathrm{r,axial}$	relative permeability in the axial direction [-]
$\mu_\mathrm{r,Fe}$	relative permeability on the non-saturated iron [-]
$\mu_\mathrm{r,PM}$	relative permeability on the permanent magnet [-]
ρ	density of air $\left[\frac{\mathrm{kg}}{\mathrm{m}^3}\right]$
ρ_mass	mass density $\left[\frac{\mathrm{kg}}{\mathrm{m}^3}\right]$
$\sigma_\mathrm{F,tan}$	air gap stress tangential component $\left[\frac{\mathrm{N}}{\mathrm{m}^2}\right]$
ϕ	phase angle $[\mathrm{rad}]$
ϕ_d	flux linkage seen by one coil side in the direct-axis direction $[\mathrm{Vs}]$
ϕ_q	flux linkage seen by one coil side in the quadrature-axis direction $[\mathrm{Vs}]$
ψ_d	direct-axis flux linkage $[\mathrm{Vs}]$
ψ_PM	flux linkage produced by the permanent magnets $[\mathrm{Vs}]$
ψ_q	quadrature-axis flux linkage $[\mathrm{Vs}]$
$\vec{\psi}_\mathrm{r}$	rotor flux linkage vector $[\mathrm{Vs}]$

$\vec{\psi}_{\mathrm{s}}$	stator flux linkage vector $[\mathrm{Vs}]$
$\vec{\psi}_{\mathrm{PM}}$	permanent magnet flux linkage vector $[\mathrm{Vs}]$
$\vec{\psi}_{\delta}$	air gap magnet flux linkage vector $[\mathrm{Vs}]$
ω	electrical angular frequency $\left[\frac{\mathrm{rad}}{\mathrm{s}}\right]$

Acronyms

DD	Direct-Driven
DFIG	Doubly Fed Induction Generator
FEM	Finite Element Method
PM	Permanent Magnet
SG	Synchronous Generator
SM	Synchronous Machine

List of publications

Publication I

J. Sopanen, V. Ruuskanen, J. Nerg, and J. Pyrhönen, "Dynamic torque analysis of a wind turbine drive train including a direct-driven permanent-magnet generator," *IEEE Transactions on Industrial Electronics*, vol. 58, no. 9, pp. 3859–3867, Sep. 2011.

Publication II

V. Ruuskanen, J. Nerg, P. Kurronen, and J. Pyrhönen, "Torque ripple reduction in direct-driven permanent magnet wind generators," *International Review of Electrical Engineering (I.R.E.E.)*, vol. 6, no. 3, pp. 1161–1173, Jun. 2011.

Publication III

J. Nerg and V. Ruuskanen, "Lumped-parameter-based thermal analysis of a direct-driven permanent magnet wind generator utilizing double radial air cooling," *Electrimacs 2011*, Cergy-Pontoise, France, Jun. 2011.

Publication IV

J. Pyrhönen, V. Ruuskanen, J. Nerg, J. Puranen, and H. Jussila, "Permanent-magnet length effects in AC machines," *IEEE Transactions on Magnetics*, vol. 46, no. 10, pp. 3783–3789, Oct. 2010.

Publication V

V. Ruuskanen, J. Nerg, and J. Pyrhönen, "Effect of lamination stack ends and radial cooling channels on no-load voltage and inductances of permanent-magnet synchronous machines," *IEEE Transactions on Magnetics*, vol. 47, no. 11, pp. 4643–4649, Nov. 2011.

Publication VI

V. Ruuskanen, P. Immonen, J. Nerg, and J. Pyrhönen, "Determining electrical efficiency of permanent magnet synchronous machines with different control methods," *Electrical Engineering*, to be published

Chapter 1

Introduction

At the moment, wind energy is one of the most promising and fastest growing renewable electric energy source. The output power of the wind turbines is continuously increasing, and multimegawatt wind turbines are already in common use. In 2009, the average installed turbine size was 1.6 MW, and the largest turbine installed was the 7.5 MW direct-driven turbine by Enercon with an electrically excited synchronous generator. The technical development is decreasing the production cost of wind energy to make wind energy compete with traditional energy sources [1]–[3].

1.1 Wind generator drive train topologies

The wind turbine systems can be manufactured using many different constructions. Overviews of different topologies are given for example in [4]–[6].

Nowadays, the most common wind turbine drive train concept contains a step-up gear and a variable-speed Doubly Fed Induction Generator (DFIG) with a partial-scale converter [7], [8]. The stator of the generator is directly connected to the grid as shown in Fig. 1.1. The wound rotor is fed by a power converter controlling the rotor slip frequency. The converter power capability can be only a fourth of the generator nominal power reducing the converter costs considerably compared with the full power converter. The speed can be varied approximately one-third above or below the synchronous speed.

The advantages of the variable-speed DFIG generator are low converter costs and quite a large speed range unlike with the fixed-speed concepts. There are yet several drawbacks. Slip rings are needed to conduct the rotor current between the converter and the rotor winding. The slip rings cause electrical and mechanical losses, and there is a regular need for maintenance. As the rotational speed of the megawatt-range wind turbine is only $10-20$ min^{-1} [9], a multistage gearbox is needed to increase the speed to be suitable for the DFIG, typically rotating

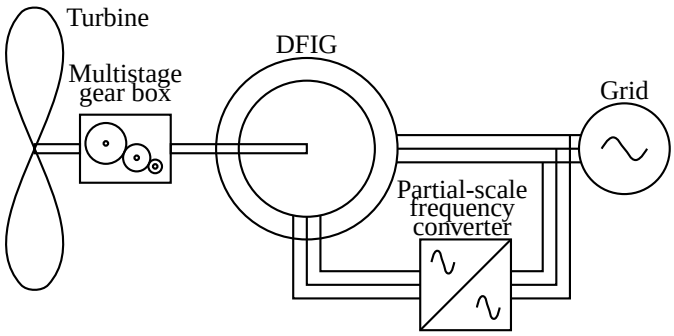

Fig. 1.1: Variable-speed wind turbine with a doubly fed induction generator.

up to $2000\ \mathrm{min}^{-1}$ [7]. The gearbox causes a large proportion of the costs and mass of the system. Typically, the cost of the generator itself is only a fraction of the costs of the gearbox [10]. The gearbox produces audible noise and considerable mechanical losses. It can be assumed that every stage of the multistage gearbox causes a power loss of 1% of the rated power [11]. Oil is needed for lubrication and it has to be replaced regularly, which increases the maintenance cost significantly especially in offshore applications. Despite regular maintenance, the gearbox is still vulnerable to faults. At present, the largest DFIG wind turbines are manufactured by Repower and are of the size of $6.15\ \mathrm{MW}$ [12].

The wind generators operate most of the time at partial load because of the varying wind speed. The power captured by the turbine is

$$P_\mathrm{t} = P_\mathrm{w} C_\mathrm{p} = \frac{1}{2} C_\mathrm{p} \rho A v_\mathrm{w}^3, \tag{1.1}$$

where P_w is the power of wind, C_p the power coefficient, ρ the density of air, A the area of the rotor of the turbine, and v_w the speed of the wind. The theoretical maximum for the power coefficient C_p is the Betz limit $C_\mathrm{p} = 16/27 \approx 0.6$ [13]. As the power of the wind is proportional to the cube of the wind speed, even a small decrease in the wind speed significantly decreases the power of the wind. Therefore, the average power of the wind turbine is typically quite low. For example, in Finland, the typical average power of a wind turbine at $100\ \mathrm{m}$ height is from 25% of the turbine nominal power in inland areas up to 50% in offshore areas [14]. The nominal power of the megawatt-range wind turbine is typically reached at wind speeds around $14\ \mathrm{m/s}$. Most of the time, the wind speed is less than $10\ \mathrm{m/s}$ even in offshore locations. The wind speed distribution graphs for several localities in Finland and other European countries can be found in [15]. In Finland, the average wind speed, at the height of $100\ \mathrm{m}$, is around $5\ \mathrm{m/s}$ in inland areas and more than $9\ \mathrm{m/s}$ can be reached only in some coastal areas [14]. This is a very inconvenient characteristic, because the electrical efficiency of the DFIG decreases substantially below the nominal load as the power of wind decreases, as shown for example in [16].

To improve the generator efficiency and eliminate the gearbox, a Direct-Driven Permanent Magnet Synchronous Generator (DDPMSG) can be used. Because of the low speed of the

turbine, very high and high-quality torque is needed to produce megawatt-range power. The PMSG is connected to the grid using a full-power converter as seen in Fig. 1.2 to enable the variable-speed operation of the PMSG.

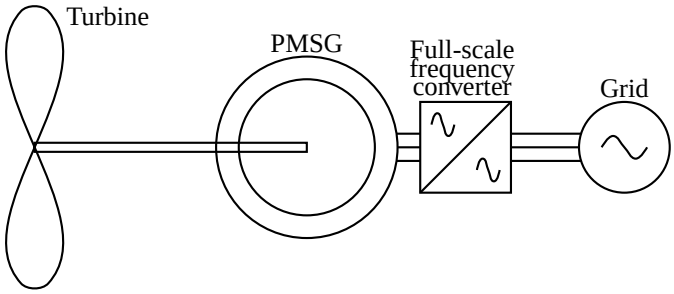

Fig. 1.2: Variable-speed wind turbine with a direct-driven permanent magnet synchronous generator.

Because of the PM excitation, there are only some eddy current losses in the rotor, and the efficiency of the DDPMSG is superior compared with the other generator types of the same speed. Especially, the partial load efficiency of the PMSG is high, because no power is needed for the excitation. A gearbox is not needed, which saves the costs and mass of the system. The large diameter, however, makes the generator itself heavy and expensive. Furthermore, a lot of costly PM material containing rare earth metals is needed. A full-power converter is more expensive and generates more losses than the partial-scale converter needed for the DFIG drive, because the nominal load losses and cost of the converter can be assumed to be directly proportional to the nominal power of the converter as in [10]. The full-power converter allows the speed of the generator and the turbine vary freely and provides an opportunity to maximize the generator efficiency at different operating points by the machine control. The converter also enables the grid connection, and therefore, no other devices are needed. The requirements for the wind power grid connection are described in the standards and the transmission system operator requirements, the most relevant of which are introduced in brief in [15]. It could, however, be stated that the full-power converter system has the most degrees of freedom to meet the network code requirements.

1.2 Constraints of the direct-driven generator design

The high torque, low rotational speed, and economic demands set strict boundary conditions for the design of the direct-driven permanent magnet synchronous generator. The high torque sets very high requirements for the torque quality of the generator. The cogging torque and the load torque ripple must be kept low enough to prevent possible mechanical failures of the power drive train.

The low rotational speed makes it necessary to use a large number of poles. The high number of poles is needed for several reasons. The electrical frequency of the machine is recommended to be kept high enough, not below 10 Hz, to avoid additional cyclic temperature

stress on the IGBTs of the converter. Increasing the pole number decreases the copper losses of the machine and the amount of the stator yoke lamination material needed. On the other hand, the number of poles is limited because the pole pitch must be large enough to fit the bar-shaped copper conductors to the stator slots. The stator slots cannot be too narrow in order to avoid the unnecessary increase in the stator flux leakage. The high pole number also decreases the pole pitch increasing the proportion of the rotor flux leakage between the side by side magnets magnetized in opposite directions.

The high torque and the large number of poles together increase the size and weight of the machine so that typically the mass of the megawatt-range wind generator is several tens of metric tons and the air gap diameter is several meters because the length of the machine is constrained by the size of the nacelle. For example, a $2.2\ \mathrm{MW}$ DDPMSG by The Switch has an outer diameter of $4.4\ \mathrm{m}$, a length of $2.8\ \mathrm{m}$, and a mass of $55\ \mathrm{t}$ [17]. To keep the physical size of the machine as small as possible in order to decrease the manufacturing and material costs, the torque density of the machine has to be maximized. The tangential air gap stress can be expressed as

$$\sigma_{\mathrm{F,tan}} = \mu_0 H_{\mathrm{n}} H_{\mathrm{tan}} = B_{\mathrm{n}} A, \tag{1.2}$$

where μ_0 is the vacuum permeability, H_{n} the field strength normal component, H_{tan} the field strength tangential component, B_{n} the flux density normal component, and A is the linear current density [18], [19]. The torque and current densities are, in practice, limited by the cooling capability of the machine. The air gap flux density fundamental wave peak value is limited to about $1\ \mathrm{T}$ by the material properties of both the permanent magnets and the stator core lamination materials. In direct-drive machines, the frequency usually remains low, and therefore, the iron losses remain limited and do not restrict the machine performance. On the other hand, although the torque density is maximized, the electrical efficiency of the machine must be as high as possible to maximize the power production capability.

The large physical size of the machine sets its own requirements. The stator of the PMSG can be divided into several segments to facilitate the manufacturing and transportation of the machine. All the parallel windings can be driven by independent low-voltage converters to maximize the power without applying high-voltage technology as the total power of the generator is divided into several converters. The segmentation also increases the reliability of the machine as all the segments can operate as independent machines despite the possible failures in the other segments, for example a malfunction in one converter does not necessarily stop the operation of the turbine.

The stator winding must be made of bar-shaped copper conductors, which makes the stator skew practically impossible. The large number of poles increases the number of stator slots, and therefore, it is impossible to use several slots per pole and phase. The torque as a function of load angle for a non-salient pole PMSM can be expressed as

$$T = \frac{3p}{\omega^2} \frac{U_{\mathrm{s}} E_{\mathrm{PM}}}{L_{\mathrm{s}}} \sin\delta, \tag{1.3}$$

where p is the number of pole pairs, ω the electrical angular frequency, U_s the stator phase voltage, E_PM the no-load voltage, L_s the stator synchronous inductance, and δ the load angle. As a very high torque is needed, the synchronous inductance must be minimized as the flux of the machine is maximized, which leads to the use of the rotor-surface-mounted NdFeB (neodymium iron boron) magnets.

The tendency to use a high number of poles and the use of rotor-surface-mounted magnets lead to a situation where the stator leakage inductance is at the same level as the magnetizing inductance. Therefore, the machine must be designed to keep the leakage at an acceptable level. The armature reaction increases the main flux of the machine, and if the armature reaction at high loads is not compensated by the demagnetizing control, the armature reaction can easily increase the stator flux causing the saturation of the main flux path and the magnetization inductance. As the leakage is not as heavily saturated as the main flux path, an increasing proportion of the main flux travels through a leakage flux path through the stator slots not producing torque.

Typically, the generator must be able to face a short-circuit situation without demagnetization of the magnets. The NdFeB magnets must be kept cool enough to handle the short circuit and avoid the loss of the remanent flux density, which decreases as a function of temperature increase. Typically, air cooling is preferred instead of water cooling because of the complexity of the water cooling system. In offshore applications, extreme reliability and a low need for maintenance is required of the cooling system.

1.3 State of the art in DDPMSGs

There are only a few companies producing megawatt-range DDPMSGs. One of the first commercially available megawatt-range DDPMSGs was the Zephyros Z72 having a nominal power of $1.5\ \mathrm{MW}$ and a nominal speed of $18\ \mathrm{min}^{-1}$ [20]. ABB is producing DDPMSGs at powers $1.5-3.0\ \mathrm{MW}$ operating at speeds $14-30\ \mathrm{min}^{-1}$ [21]. It is said that the DDPMSG has the lowest maintenance demand of all the wind generators by ABB. Siemens is producing DDPMSGs at powers $2.3-3.0\ \mathrm{MW}$ operating at speeds $6-16\ \mathrm{min}^{-1}$ [22]. The nacelle mass of the Siemens DDPMSGs is $73\ \mathrm{t}$. The Switch is producing the DDPMSGs at powers $1.65-4.25\ \mathrm{MW}$ with nominal operating speeds between $16-18\ \mathrm{min}^{-1}$ [17]. The generators by The Switch are available with either inner or outer rotors.

The research activity has been quite intense related to the PM generators and also with the DDPMSGs over the last few years. Several different machine topologies have been investigated [9], [23]–[26]. The cogging torque reduction methods are studied in [27]. However, only a few studies deal with the megawatt-range generators. Dubois compared the different PM generator topologies with each other [28]. Grauers showed that the DDPMSGs are more efficient than the conventional wind generator drive trains and that the DDPMSG drive train needs only a slightly larger nacelle than the geared solutions [29]. The numbers of poles and slots were studied in [30]. Different rotor geometries were compared in [31]. The new control strategy for a $2\ \mathrm{MW}$ DDPMSG is presented in [32]. The $10\ \mathrm{MW}$ DDPMSG applying active speed stall control is introduced in [33].

1.4 Machine studied

In this doctoral thesis, a $3.35\ \mathrm{MW}$ DDPMSG by The Switch [34] is used as a basis. The machine has a nominal speed of $16\ \mathrm{min}^{-1}$ and a nominal torque of approximately $2\ \mathrm{MNm}$. As there are 120 poles in the machine, the nominal frequency is $16\ \mathrm{Hz}$. The stator outer diameter of the machine is approximately $6\ \mathrm{m}$. The active length of the machine is $1.2\ \mathrm{m}$. The mass of the $4.25\ \mathrm{MW}$ production version of the machine is $84\ \mathrm{t}$.

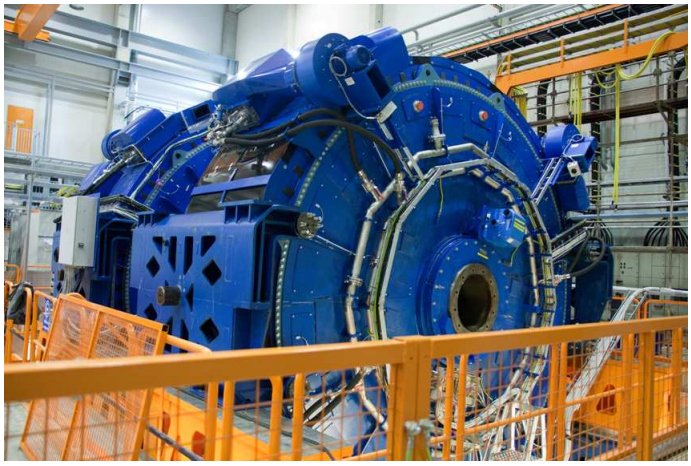

Fig. 1.3: $4.25\ \mathrm{MW}$ *direct-driven PMSGs under back-to-back test. Photo courtesy of The Switch.*

The stator of the machine is divided into 12 independent electrically parallel segments. Each segment has 10 poles and 30 stator slots, and therefore, the number of slots per pole and phase is one, $q = 1$. The winding is made of bar-shaped copper conductors, which form a two-layer three-phase winding providing a short end winding. As the stator segments are independent of each other, the winding cannot reach across two segments, and thus, there are three only half-filled slots at both ends of the stator segment. There are three parallel converters, all of them controlling four parallel stator segments each having the nominal main voltage of $690\ \mathrm{V}$.

The machine carries NdFeB magnets mounted on the rotor surface. The magnets are sinusoidally shaped to decrease the 5^{th} and 7^{th} harmonics of the rotor current linkage. The magnets are placed in rows of twelve magnets in the axial direction. Along the air gap magnets, the rows are slightly overlapping to emulate the skew and to reduce the cogging torque. The remanent flux density of the magnets is $1.2\ \mathrm{T}$, and the magnets cover 80% of the rotor surface.

Because of the low rotational speed and frequency, the iron losses of the machine are low. The iron losses are only one-tenth of the amount of the stator copper losses. That is why the cooling system is designed to maximize the stator winding cooling. The doubly radial cooling is applied where the stator is divided into several substacks in the axial direction, and there are cooling ducts between each substack. The air is forced from axial, high-pressure cooling

channels behind the stator yoke area radially through the cooling duct to the air gap. In the air gap, the air moves mainly tangentially to the next cooling duct, where it travels again radially from the air gap through the stator to the next, low-pressure axial cooling channel behind the stator yoke area.

The machine has been extensively tested by The Switch during the process, and the close co-operation has guaranteed the necessary feedback for the researchers. However, the confidentiality requirements set by the collaborating company limit the right to publish any experimental results in this thesis.

1.5 Outline of the thesis

The target of the work is to draw up guidelines on the design of high-performance megawatt-range direct-driven permanent magnet generators. In the design, there are two aspects that have been studied.

The first area to be studied is the torque quality. Several torque quality improvement methods are studied and compared with each other.

The second research area is the effects of the torque density maximization in the DD generators. This target leads to the requirement of maximizing the air gap flux density and the linear current density, which again leads to the requirement of using radial cooling ducts and dividing the lamination stack into several substacks. The effect of substacking on the PM flux and the inductances of the machine is studied.

The stator voltage maximizing the efficiency of the DDPMSG is studied over the operational speed and torque range. It is discovered that both the control maximizing the efficiency and substacking have a tendency to strengthen the armature reaction leading to the saturation of the stator lamination at high loads. The effect of the lamination material saturation on the machine efficiency is observed.

This doctoral thesis consists of the introductory part and six original publications. The structure of the introduction is divided into seven chapters providing conclusions of the relevant publications.

In Chapter 1, a short introduction to the megawatt-range permanent magnet synchronous generators is given. The state of the art of the DDPMSGs is introduced, and finally, the machine studied in the thesis is introduced.

In Chapter 2 and **Publications I** and **II**, the torque quality of the DDPMSGs is discussed. The cogging torque and load torque ripple mechanisms are introduced. The limits for the acceptable torque ripples are presented. Several methods to reduce the cogging torque and the load torque ripple are studied. The studied methods are the shaping of the rotor surface, magnet skew, magnet shaping, and asymmetric placement of the magnets or stator slots. The

methods are compared with each other in terms of the torque quality, generator efficiency, and manufacturing. The best methods to reduce torque ripple are suggested.

The torque ripple reduction techniques were studied and the results were reported by the author of the thesis. The mechanical model of Publication I was developed and the mechanical analysis carried out by Dr. Jussi Sopanen. The torque ripple components used as the input for the mechanical model were calculated by the author. The analytical model of the induction of torque ripple components in the case of asymmetries in the machine was produced by the author. The author wrote the manuscript of Publication II and participated in writing the sections concerning the torque ripple produced by the PMSG in Publication I with Dr. Janne Nerg.

In Chapter 3 and **Publication III**, the heat transfer of the air-cooled PMSG is discussed. The thermal lumped-parameter model is described for the steady-state and transient analysis. Several combinations of the number of the radial cooling ducts and the width of the ducts are studied. The temperature distribution and the flow rate of air in the different parts of the machine are investigated. It is found that a large number of radial cooling ducts are needed for the air cooling of the DDPMSG.

The thermal model was originally constructed by Dr. Janne Nerg. The model was modified by the author to simulate the transient states. The model was improved by the author to calculate the temperature distribution of the machine with a variable number and width of radial cooling ducts affecting also the amount of copper losses of the machine. By the improved model, the author determined the allowable combinations of the number and width of the radial cooling ducts for the DDPMSG studied.

In Chapter 4 and **Publication IV**, the effect of radial cooling ducts and the end effects on the PM flux and the effective length of the PMSG is studied with the 2D Finite Element Method. The method to estimate the effective length by integrating the flux density in the air gap of a 2D cross-section of the machine is developed and applied. The method to compensate the permanent magnet end leakage by making the magnets slightly longer than the stator stack is presented.

The problem was originally formulated by Prof. Juha Pyrhönen. The method to calculate the effective stack length with the 2D FEM was developed by the author. The results were found and the conclusions made by the author. The publication manuscript was written by Prof. Juha Pyrhönen and Dr. Janne Nerg, who also reproduced the results provided by the author. The method developed was also applied to an axial flux machine, and the results were published in [35].

In Chapter 5 and **Publication V**, the effect of the radial cooling ducts on the no-load voltages and synchronous inductances of the PMSGs is studied with the 3D FEM. The effects of extending the magnets are analyzed with several geometries. The saturation effects on the PM end flux leakage compensation and the synchronous inductances as a function of stator current are investigated with different air gap flux densities.

The models were built and the calculations were carried out by the author. The author also made the conclusions and wrote the manuscript of the publication.

In Chapter 6 and **Publication VI**, the different control methods of PMSGs are compared with each other. The control methods are applied to both salient and non-salient pole PMSMs. An analytical model to determine the efficiency of the PMSG over the whole speed and torque range applying several control methods is developed. The voltage rise caused by the armature reaction when using the $i_{\mathrm{d}} = 0$ control is studied. As an addition to the Publication VI, the effect of inductance saturation on the machine performance is studied in this thesis.

The algorithm was made and the publication manuscript written in co-operation with Ms Paula Immonen, M.Sc. The results dealing with the wind generators were calculated by the author and the results dealing with the hybrid drive machine by Ms Immonen. The author improved the model by adding the option to take the inductance saturation into account.

In Chapter 7, the scientific contributions of the doctoral dissertation are discussed and suggestions are given for the future work.

1.6 Scientific contributions

The main scientific contributions of the thesis are the following:

1. Comparative analysis of the torque ripple reduction methods from the perspective of megawatt-range DDPMSGs.
2. Development of an analytical tool to estimate the torque ripple of the DDPMSG with different current linkage distributions including the asymmetries of the machine geometry.
3. Analytical analysis of the effect of the number and width of cooling ducts on the electromagnetic and thermal performance of the doubly radially cooled DDPMSG.
4. Development of the method to calculate the effective length of the PMSM with the FEM by applying the axial cross-section of the machine.
5. Proposal and verification of the method to compensate the loss of the PM flux caused by the stack end area leakage by making the magnets longer than the stator substacks.
6. Analysis of the effect of radial cooling ducts on the effective length of the PMSM with the 2D and 3D FEM.
7. Analysis of the effect of radial cooling ducts on the no-load voltage and inductances of the PMSM with the 3D FEM.
8. Development of an analytical algorithm to calculate the efficiency of the PMSM over the whole speed and torque plane with several control methods.
9. Implementing the effect of the inductance saturation on the analytical algorithm to calculate the efficiency of the PMSM and to analyze the effect of inductance saturation on the PMSMs.

Chapter 2

Torque quality

The high torque and low rotational speed of the direct-driven permanent magnet synchronous generators set high demands on the torque quality, because in direct drives the mechanical system has poorly damped resonances at the torque ripple frequencies. The torque ripple is divided into cogging torque and load torque ripple. The cogging torque is a consequence of the varying permeance of the magnetic circuit, and the load torque ripple is excited by the flux harmonics produced by the stator current.

There are several factors affecting the torque quality of the DDPMSGs. The winding of the DDPMSG studied has only one slot per pole and phase. Hence, the winding produces lots of harmonics, and it is not possible to use short pitching to reduce the harmonics. Furthermore, the only half-filled slots at the edges of the stator segments induce subharmonic components to the stator current linkage. The bar-shaped winding practically prevents the use of the stator skew and shaping of the stator slot. The rectangular rotor-surface-mounted magnets best covering the rotor area produce a rectangular-shaped current linkage including all the odd harmonic components described as

$$x = \frac{4}{\pi} \sum_{k=1}^{\infty} \frac{\sin((2k-1)2\pi f t)}{2k-1}, \tag{2.1}$$

where k is the order of harmonic.

The torque of the electrical machine can be presented as a cross product of the machine flux linkage components

$$T = \frac{3p}{2} |\vec{\psi}_{\mathrm{s}} \times \vec{i}_{\mathrm{s}}| = \frac{3p}{2} \frac{1}{L_{\mathrm{s}}} |\vec{\psi}_{\mathrm{r}} \times \vec{\psi}_{\mathrm{s}}|, \tag{2.2}$$

where p is the number of pole pairs, $\vec{\psi}_{\mathrm{s}}$ the stator flux linkage space vector, $\vec{i}_{\mathrm{s}}$ the stator current space vector, L_{s} the stator synchronous inductance, and $\vec{\psi}_{\mathrm{r}}$ the rotor flux linkage space

vector equal to the permanent magnet flux linkage space vector $\vec{\psi}_{\mathrm{PM}}$. All the other terms are real multipliers, and thus, the torque harmonics can be observed by analyzing the cross product only. The space vectors describing the direction and amplitude of the individual sinusoidally distributed machine quantity components or sums of the sinusoidally distributed components are simply called vectors later on in this thesis. The most important harmonic flux components produced by the winding and the rectangular surface magnets are the 5^{th} and 7^{th} harmonic. At the stator, the 5^{th} harmonic is traveling in the opposite direction with a speed of one-fifth compared with the fundamental wave. The 7^{th} harmonic is traveling in the same direction with a speed of one-seventh compared with the fundamental wave [19]. If the permeance variations are ignored, it is possible to represent the PM flux density distribution by a Fourier series depending on the rotor periphery position. As the rotor rotates, the Fourier series components are seen by the stator as time-varying components that all have the same peripheral speed as the rotor itself. The stator and rotor flux densities containing the fundamental wave, the 5^{th} harmonic, and the 7^{th} harmonic are presented as complex phasors as follows

$$\vec{B}_{\mathrm{s}} = s_1 \mathrm{e}^{(\omega t+\theta)\mathrm{j}} + s_5 \mathrm{e}^{(5\theta-\omega t)\mathrm{j}} + s_7 \mathrm{e}^{(7\theta+\omega t)\mathrm{j}}, \tag{2.3}$$

$$\vec{B}_{\mathrm{r}} = r_1 \mathrm{e}^{(\omega t+\theta+\delta)\mathrm{j}} + r_5 \mathrm{e}^{(5\theta+5\omega t+5\delta)\mathrm{j}} + r_7 \mathrm{e}^{(7\theta+7\omega t+7\delta)\mathrm{j}}, \tag{2.4}$$

where θ describes the position change along the air gap and ωt the change as a function of time. The terms s_1, s_5, s_7, r_1, r_5, and r_7 denote the amplitudes of the stator and rotor harmonics. The cross product of the flux densities is

$$\begin{aligned}
\vec{B}_{\mathrm{s}} \times \vec{B}_{\mathrm{r}} = \; & s_1 r_1 \sin(\delta) \cdots \\
& + s_1 r_5 \sin(4\theta + 4\omega t + 5\delta) \cdots \\
& + s_1 r_7 \sin(6\theta + 6\omega t + 7\delta) \cdots \\
& + s_5 r_1 \sin(-4\theta + 2\omega t + \delta) \cdots \\
& + s_5 r_5 \sin(6\omega t + 5\delta) \cdots \\
& + s_5 r_7 \sin(2\theta + 8\omega t + 7\delta) \cdots \\
& + s_7 r_1 \sin(-6\theta + \delta) \cdots \\
& + s_7 r_5 \sin(-2\theta + 4\omega t + 5\delta) \cdots \\
& + s_7 r_7 \sin(6\omega t + 7\delta).
\end{aligned} \tag{2.5}$$

By integrating the cross product over one pole pair $\theta = [0, 2\pi]$, several terms are canceled because the multiplier of θ is an integer. The cross product after cancellation is

$$\begin{aligned}
\vec{B}_{\mathrm{s}} \times \vec{B}_{\mathrm{r}} = \; & s_1 r_1 \sin(\delta) \cdots \\
& + s_5 r_5 \sin(6\omega t + 5\delta) \cdots \\
& + s_7 r_7 \sin(6\omega t + 7\delta).
\end{aligned} \tag{2.6}$$

It can be seen that the 5^{th} and 7^{th} harmonic both produce the 6^{th} torque harmonic. Let us now study the cross product of two flux components with the harmonic orders a and b, which can also be fractional numbers smaller than one in the case of subharmonic flux components. The multiplier of the time term of the rotor harmonic is the same as the order of the harmonic because the rotor harmonic, induced by the permanent magnets, is traveling at the same speed as the fundamental wave. The stator wave is traveling at a speed proportional to the harmonic order so that the time term is ωt and the direction is described with the sign of the time term. The stator and rotor flux components are

$$\vec{B}_{\mathrm{s}} = s_a \mathrm{e}^{(a\theta \pm \omega t)\mathrm{j}}, \tag{2.7}$$

$$\vec{B}_{\mathrm{r}} = r_b \mathrm{e}^{(b\theta + b\omega t + b\delta)\mathrm{j}}. \tag{2.8}$$

Now, the cross product is

$$\vec{B}_{\mathrm{s}} \times \vec{B}_{\mathrm{r}} = s_a r_b \sin([b-a]\theta + [b \mp 1]\omega t + b\delta). \tag{2.9}$$

If the machine has a large number of poles, the place term with the coefficient $b - a$ gets a zero value, when θ is integrated over the whole machine. That is why also in the case of subharmonics the same subharmonic component must exist in the stator and the rotor $a = b$. Hence, to mitigate torque harmonics, it suffices to remove the harmonic components either from the stator or from the rotor. The frequency of the torque harmonic induced by the stator and rotor harmonics with the harmonic frequency b has a frequency $b \mp 1$, where the sign is determined by the traveling direction of the stator harmonic.

The low rotational speed and supply frequency keep the frequency of the torque ripple moderate. The low frequency of the torque ripple is problematic because the resonance frequencies of the DDPMSGs are also low as shown in Publication I. The resonance frequency of the DDPMSG drive train is mainly determined by the properties of the shaft and the turbine. In this case, the turbine is modeled as a rigid body, and the changes in the inertia of the turbine do not have a significant effect because the turbine inertia is two decades as high as the inertias of the rotor of the PMSG. In the case of the DDPMSGs, the torque ripple is less harmful if the frequency is increased. It was found out that the most problematic torque ripple is the cogging torque, because the resonance frequencies are matched during the startup below the nominal speed, where the load torque of the generator is low, but the cogging torque is independent of the load torque.

2.1 Torque ripple reduction methods

Several methods to reduce torque ripple are introduced in the literature. In this section, only the methods suitable for DDPMSGs are investigated. Methods to reduce the cogging torque

by lamination shaping of the PMSM with rotor-buried magnets have recently been presented in [36]–[38]. The effect of skew has been widely studied on different types of permanent magnet machines [39]–[46]. Modifying the air gap flux waveform with surface-mounted magnets by shaping the magnets is described for example in [46], [47]. The asymmetrical magnet placement is investigated for cases where it is not possible to use skew [48]–[50]. The asymmetrical placement of the stator slots is introduced in [51].

In the following sections, several methods to decrease the torque ripple are introduced in brief. The benefits and drawbacks of the methods are discussed. The torque quality of the methods presented are compared with each other in Publication II.

2.1.1 Rotor-buried magnets

By burying the magnets inside the rotor lamination it is possible to affect the shape of the air gap flux by shaping the rotor laminate on the magnets. An almost sinusoidal air gap flux can be achieved even with rectangular magnets. At the same time, the magnet can easily be isolated from the surrounding air and additional fastening of the magnets is not needed. Magnets are also better protected against demagnetization during possible short-circuit situations, although the short-circuit demagnetization is typically not an issue with the DDPMSGs with a large magnetic air gap, large leakage inductance, and small magnetizing inductances.

On the other hand, the lamination of the rotor surface increases the mass of the rotor considerably, because the lamination is not able to be part of the mechanical support structure as the solid steel rotor is. As there is high-permeability laminate material around the magnets, the amount of rotor leakage flux increases. Magnet material is wasted to magnetize the necks of the lamination material between and along the magnets providing the mechanical support for the lamination material on the magnets. The rotor-buried magnets typically cause negative saliency ($L_\mathrm{d} < L_\mathrm{q}$) to the machine. The quadrature-axis inductance can be decreased by shaping the air gap in the quadrature-axis area.

2.1.2 Magnet skew

Because it is not possible to skew the stator winding in the case of the bar-shaped conductors, the skew can be used in the rotor by magnet placing. In large-scale PMSGs, it is practically impossible to produce continuous skew in the rotor but magnets can be divided into several rows in the axial direction that are slightly shifted as shown in Fig. 2.1. It was found out that two rows give almost as good results as several rows, but placing the magnets in two rows eases the manufacturing process.

The no-load voltage decreases a little when using skew, although the stacking factor of the rotor does not change. The no-load voltage is reduced because the fluxes produced by the different parts of the machine are in a phase shift defined by the amount of skew. Typically, the decrease in the no-load voltage is a couple of percents because of the magnet skew.

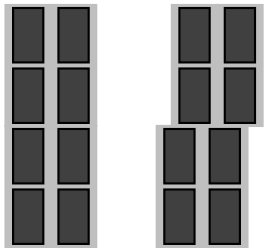

Fig. 2.1: Magnet placement geometries with rectangular rotor-surface-mounted magnets; a) without skew b) with the two-row skew.

The two-row skew is a powerful tool to decrease the cogging torque. In the case of the two-row skew, the magnet rows are shifted half of the stator slot pitch from each other. The amplitude of the cogging torque can be decreased to a fraction of the cogging of the non-skewed machine. The frequency of the cogging torque is doubled in the case of the two-row skew, which is beneficial in DDPMSGs. The skew decreases the load torque ripple also, but the amplitude is not decreased as much as the cogging torque amplitude, and the frequency of the lowest load torque ripple harmonic component is not doubled.

2.1.3 Magnet shaping

With the surface-mounted magnets, the only way to affect the shape of the current linkage distribution produced by a single magnet is to shape the magnet itself. The magnets can be shaped to produce a sinusoidal current linkage in the tangential or axial direction. By shaping the magnet, several harmonics can be canceled from the flux linkage distribution produced by the magnet. Because the amount of magnet material and the rotor stacking factor are decreased, part of the no-load voltage is lost. To increase the rotor stacking factor, the third harmonic shape can be added to the magnets as shown in Fig. 2.2, because the third harmonic effects are canceled in the three-phase systems. The magnet shaping has been patented by Prof. Pyrhönen and The Switch [52].

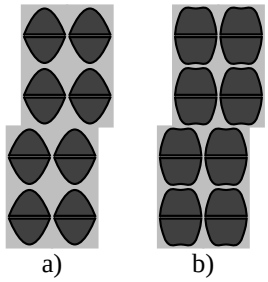

Fig. 2.2: Shaped rotor-surface-mounted magnets with skew; a) pure sinusoidal magnets b) the 3^{rd} *harmonic added.*

The shaping of the magnets does not change the assembly process. With sinusoidal magnets it is also possible to use magnet skew similarly as with the rectangular magnets.

It was discovered that the magnet shaping decreases the harmonics of the machine so much that the torque quality is very good even without skew. With the skew, the shaped magnets give almost as good torque quality as the rotor-buried rectangular magnets with skew. The use of skew is highly recommended because the frequency of the cogging torque can be doubled also in the case of the shaped magnets.

2.1.4 Asymmetric magnet placement

In some cases, it is difficult or impossible to use skew. Some kind of a skew effect can be achieved by placing magnets asymmetrically. For example, magnets in one segment are set a little closer to each other than the whole pole pitch, and some free space is left at the edges of the segments as shown in Fig. 2.3. There are numerous ways to place the magnets. Obviously, the free space implementing the asymmetry decreases the fundamental winding factor and the no-load voltage. Also the stacking factor of the rotor surface can be decreased, because narrower magnets may be required to assemble the magnets more densely than in the case of the symmetrical placement.

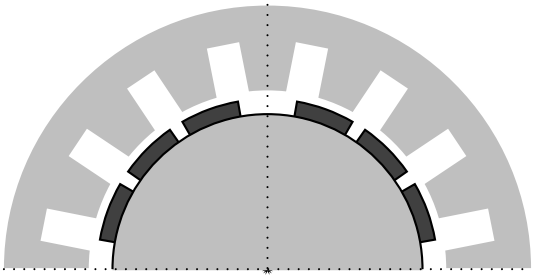

Fig. 2.3: Principle of the magnet asymmetry of the machine with four stator segments.

The asymmetric magnet placement significantly reduces the cogging torque amplitude, but it is not able to multiply the main cogging torque ripple frequency as the skew does. The main drawback of the asymmetric magnet placement is the subharmonic flux components induced by the magnet asymmetry. The effects of the subharmonic components were analyzed analytically to explain the results achieved with the FEM.

The analytical calculation was performed by starting with the current linkage waveforms of the stator and the rotor as a function of time and place along the air gap. For every time step, the current linkages were expressed as a sum of harmonic components. The current linkage waveforms for one moment of time are presented in Fig. 2.4. As the harmonic components were known as a function of time, the torque was calculated for every time step and place as a cross product neglecting the scalar coefficient term of (2.2). The torque of the machine for every time step was calculated by integrating the torque components over the segment or the whole machine.

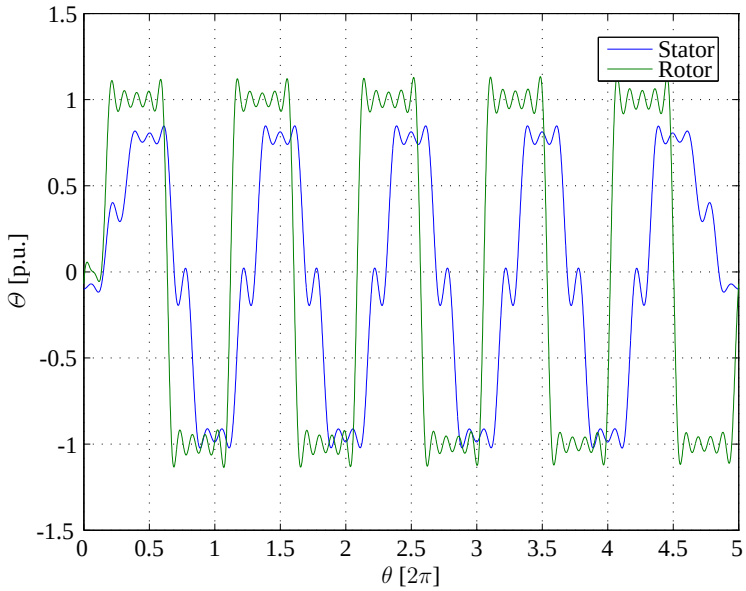

Fig. 2.4: Sums of the lowest harmonics of the stator and rotor current linkage over one segment with asymmetric magnet placement. The asymmetry in the rotor current linkage can be seen near the zero angle. The effect of the half-filled stator slots can be seen from the outermost current linkage edges that differ from the others and from the offset of the current linkage at the observed time step.

The amplitudes of the flux components produced by the permanent magnets do not change as a function of time. The rotor subharmonics are especially harmful because there are half-filled slots in the segment edge areas in the stator, which also produce subharmonic flux components. The amplitude of the stator subharmonic components is varying as a function of time but the amplitude of the fundamental is constant. Because there are subharmonic flux components in the rotor and the stator circuit, there are also subharmonic load torque components. Typically, the subharmonic torque components are intolerable in the DDPMSGs.

2.1.5 Asymmetric stator slot placement

Subharmonic torque components are induced if there are subharmonic flux components both in the stator and in the rotor. It is also possible to imitate skew by placing the stator slots asymmetrically and keeping the rotor symmetric as shown in Fig. 2.5.

In the analytical analysis described above, it was found out that the asymmetric placement of the slots and the half-filled slots at the edges of the segment induce both the subharmonic and harmonic low-frequency multiples of the fundamental wave. Also the amplitude of the harmonics and the fundamental wave change as a function of time. The stator current linkage waveform and the sum of the lowest harmonic components at one moment of time are presented in Fig. 2.6. Also the fundamental wave and one subharmonic component are presented.

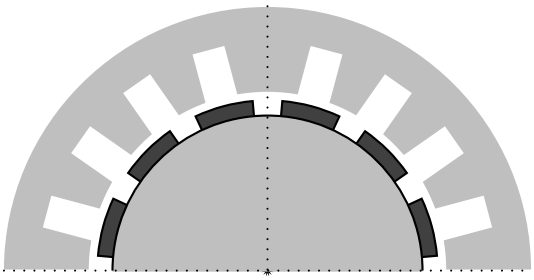

Fig. 2.5: Principle of the stator slot asymmetry of the machine with four stator segments.

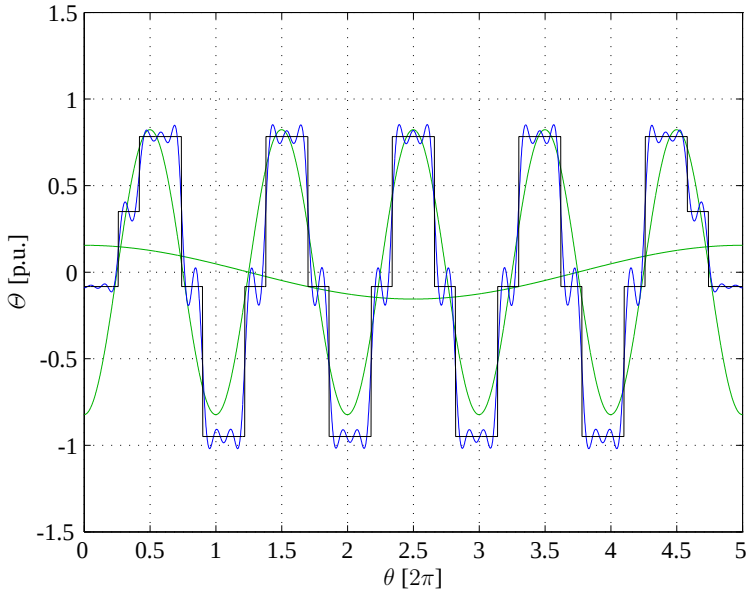

Fig. 2.6: Stator current linkage stair curve (black) and the sum of the first ten harmonics of the current linkage (blue) over one segment with asymmetrically placed stator slots. The fundamental wave and a subharmonic component with a wavelength five times the fundamental wavelength are presented in green. The effect of the half-filled stator slots is demonstrated by the fact that the amplitudes of the outermost current linkage steps are only half the amplitude of the other steps and by the offset of the current linkage at the observed time step. The effect of the asymmetrical slot placement is shown by the longer current linkage plateaus at the edges of the segment and by the fact that the phase shift between the stair curve and the fundamental wave increases towards the segment edge areas.

Now, there is asymmetry in the stator only, and thus, there are no subharmonics on the rotor side. Therefore, the stator subharmonics do not produce subharmonic torque components. The lowest torque ripple component is caused by the time variation of the fundamental wave amplitude, which is the second harmonic in the studied case.

With asymmetric stator slots, subharmonic torque components are not induced, but the load torque ripple is at a lower harmonic than without skew. In this case, the orders of harmonics

are 2, 4, and 6 in the order of decreasing amplitude. The frequency of the cogging torque is not doubled. The stator slot asymmetry is a useful tool to reduce the cogging torque amplitude, but the existence of low-harmonic load torque components must be considered.

2.2 Conclusions

The torque of the DDPMSG should be very smooth. The cogging torque is the most harmful torque ripple component. For the DDPMSGs, the torque ripple is less harmful, the higher the frequency of the ripple is.

By burying the magnets inside the shaped rotor lamination, the torque quality can be improved compared with the rotor surface magnets, but the mass and leakage of the rotor are both increased. The shaping of the magnets significantly reduces the torque ripple, but also reduces the air gap flux as less magnetic material is used on the rotor surface.

In particular, the magnet skew significantly reduces the cogging torque and multiplies the frequency of the main cogging torque component as the skew is used by assembling magnets in several rows slightly shifted from each other. Application of the magnet skew is recommended whenever possible.

If it is impossible to apply skew, it can be imitated by producing asymmetry in the rotor or in the stator. Cogging can be reduced, but the frequency of the cogging torque main component remains unchanged. The asymmetric placement of magnets is typically not allowed because of the subharmonic torque components with a relatively large amplitude. The asymmetric placement of the stator slots can be used if the low-order harmonic components at the load torque are allowed.

Chapter 3

Heat transfer

Heat transfer is among the most critical aspects when designing an electrical machine, because the cooling capability eventually determines the loading capability of the machine. The operating temperature of the machine is limited because of the heat endurance of the insulations, and in the PM machines, in particular because of the maximum operating temperature of the magnets without demagnetization.

Traditionally, electrical machines have been cooled with a forced air flow by using a blower assembled on the machine shaft. The stator core is directly air cooled and the air flow can also be steered through the ventilation channels into the machine air gap to directly cool the surface of the rotor. Liquid cooling is also used because of the notably higher heat transfer capability compared with air cooling. The stator outer surface can be liquid cooled or the cooling channels can go through the stator lamination stack [53]. Direct water cooling of the stator windings has been patented but not widely used in the wind turbine generators [54]. The stator winding is made of copper pipes with water flowing inside.

In low-speed DDPMSGs, up to 90% of the losses are generated in the stator winding, because the low frequency keeps the iron losses of the machine low. The rotor losses of the PMSM are typically low, but some losses are induced in the magnets because of the flux pulsation. The direct forced air cooling of the rotor is needed to keep the temperature of the magnets low enough. The decrease in the temperature increases the remanent flux density and the coersive force of the magnets increasing the machine performance and improving the short-circuit ride-through capability without demagnetitization of the magnets.

In the studied machine, a doubly radial air cooling described in Publication III is used. The doubly radial cooling provides powerful heat transfer for the stator winding because the cooling air flow travels between the stator winding bars in the stator cooling ducts both in the cold and hot air ducts. The magnets are effectively cooled because the air flow travels from the cold air duct to the hot air duct through the air gap. On the other hand, magnets are mounted on the massive rotor core with a large heat transfer area at the rotor inner surface. The drawback of the doubly radial cooling is the fact that the magnets are cooled with the air

that already is heated to some extent when passing through the stator. Because of this, quite a large amount of air has to be flowing in the machine as only a limited temperature difference can be allowed for the cooling air.

3.1 Thermal resistance network

Heat transfer network models are used in the thermal modeling of the machines [55], [56]. The thermal resistance network model can estimate the temperature distribution of the machine both in the steady state and during the transient states. The lumped-parameter-based thermal resistance network model for radial flux electrical machines is described in [57].

The temperature rise of each node compared with the reference temperature can be expressed as

$$\Delta \mathbf{T} = (\mathbf{G} + \mathbf{G}_{\text{fluid}})^{-1}\mathbf{P}, \tag{3.1}$$

where $\mathbf{G}$ is the thermal conductance matrix, $\mathbf{G}_{\text{fluid}}$ the cooling matrix, and $\mathbf{P}$ the loss vector containing the power loss of each node. The thermal conductance matrix $\mathbf{G}$ is defined as

$$\mathbf{G} = \begin{bmatrix} \sum_{i=1}^{n} \frac{1}{R_{1,i}} & -\frac{1}{R_{1,2}} & \cdots & -\frac{1}{R_{1,n}} \\ -\frac{1}{R_{2,1}} & \sum_{i=1}^{n} \frac{1}{R_{2,i}} & \cdots & -\frac{1}{R_{2,n}} \\ \vdots & \vdots & \ddots & \vdots \\ -\frac{1}{R_{n,1}} & -\frac{1}{R_{n,2}} & \cdots & \sum_{i=1}^{n} \frac{1}{R_{n,i}} \end{bmatrix}, \tag{3.2}$$

where the elements in the diagonal are the sums of the conductances $(\mathrm{W/K})$ connected to that node. The other conductances $\mathbf{G}(i,j)$ are the thermal conductances connected to the nodes i and j. The cooling flow can be expressed as a thermal resistance to construct the cooling matrix

$$R_{\text{q}} = \frac{1}{\rho_{\text{mass}} q_{\text{v}} c_{\text{p}}}, \tag{3.3}$$

where ρ_{mass}, q_{v} and c_{p} are the mass density $\left(\mathrm{kg/m^3}\right)$, the volume flow rate $\left(\mathrm{m^3/s}\right)$ and the specific heat capacity $(\mathrm{J/(kgK)})$ of the cooling fluid, respectively. The cooling matrix is

$$\mathbf{G}_{\text{fluid}} = \begin{bmatrix} \frac{1}{R_{\text{q}11}} & 0 & \cdots & 0 \\ -\frac{1}{R_{\text{q}21}} & \frac{1}{R_{\text{q}22}} & 0 & \vdots \\ \vdots & \vdots & \ddots & \vdots \\ -\frac{1}{R_{\text{q}n1}} & -\frac{1}{R_{\text{q}n2}} & \cdots & \frac{1}{R_{\text{q}nn}} \end{bmatrix}, \tag{3.4}$$

where $R_{\mathrm{q}ii}$ is the thermal resistance $(\mathrm{K/W})$ of the cooling fluid passing the node i and $R_{\mathrm{q}ij}$ is the thermal resistance of the cooling fluid between nodes i and j.

To analyze the transient states, the cooling capacitance matrix is needed. The thermal capacitance for each element is defined as

$$C_{\mathrm{th},i} = \sum_{j=1}^{n} m_j c_{\mathrm{p},j}, \tag{3.5}$$

where m is the mass (kg) and c_{p} the material specific heat capacity $(\mathrm{J/(kgK)})$ of the element. The index j represents the different materials of the element. The thermal capacitance matrix is

$$\mathbf{C} = \begin{bmatrix} C_{\mathrm{th},1} & 0 & \cdots & 0 \\ 0 & C_{\mathrm{th},2} & \cdots & 0 \\ \vdots & \vdots & \ddots & \vdots \\ 0 & 0 & \cdots & C_{\mathrm{th},n} \end{bmatrix}. \tag{3.6}$$

The temperature differences during the transient states are found by solving the differential equation of the temperature difference

$$\frac{\mathrm{d}}{\mathrm{d}t}\Delta\mathbf{T} = \mathbf{C}^{-1}(\mathbf{P} - (\mathbf{G} + \mathbf{G}_{\mathrm{fluid}})\Delta\mathbf{T}). \tag{3.7}$$

3.2 Results

The steady state of the machine was studied with a constant number and width of cooling ducts. It was found that the highest temperature of the machine is reached in the windings where the most of the losses are generated. The rotor circuit of the machine remains relatively cool, around $70\ ^{\circ}\mathrm{C}$, as the temperature of the inlet air is $40\ ^{\circ}\mathrm{C}$ and the temperature of the outlet air is just below $60\ ^{\circ}\mathrm{C}$, and the temperature of the magnets is low enough. The highest speed of the air flow is observed in the cooling ducts at the stator teeth area where the slot wedge narrows the teeth, and there is a spacer keeping the duct open as shown in Fig. 1 in Publication III.

In the transient analysis during the machine startup, it was discovered that the time constant of the rotor circuit is much larger than the time constant of the stator. The low temperature rise of the rotor is a consequence of the high thermal capacity and the low losses of the rotor. During the shutdown of the machine, a cooling-down of the machine is detected with the blower turned off. After the shutdown, the temperature of the winding decreases rapidly because the ohmic losses are no longer affecting. The temperature of the stator teeth and the yoke increase until they nearly reach the winding temperature, because the stator cooling is

significantly decreased by the turning off of the blower, and the inner heat of the winding spreads to the stator teeth and the yoke as a result of conduction. The temperature of the magnets does not increase, although the temperature of the stator is significantly higher than the temperature of the rotor and there is no air flow in the air gap. The temperature of the magnets is continuously decreasing because the air gap effectively isolates the rotor circuit from the stator, and the rotor circuit is cooled down through the large rotor inner surface.

The effect of the number of cooling ducts and the cooling duct width was investigated by varying them under certain boundary conditions. The number of channels should not exceed 35, and the width of ducts cannot be less than $2\ \mathrm{mm}$. Because the axial length of the machine is $1.2\ \mathrm{m}$, 35 cooling channels would mean the substack length to be $33\ \mathrm{mm}$. The maximum temperature of the winding was set to $120\ ^{\circ}\mathrm{C}$ and for the magnets to $70\ ^{\circ}\mathrm{C}$. The copper losses of the stator winding are limited to less than $160\ \mathrm{kW}$. The maximum allowable flow rate in the cooling duct was set to $35\ \mathrm{m/s}$ and the total volume flow rate of the machine was kept constant. It was found that the cooling duct width and the number combinations meeting all the requirements have a number of ducts between 18 and 24 as shown in Fig. 3.1. The cooling duct width was between $5.5\ \mathrm{and}\ 9\ \mathrm{mm}$.

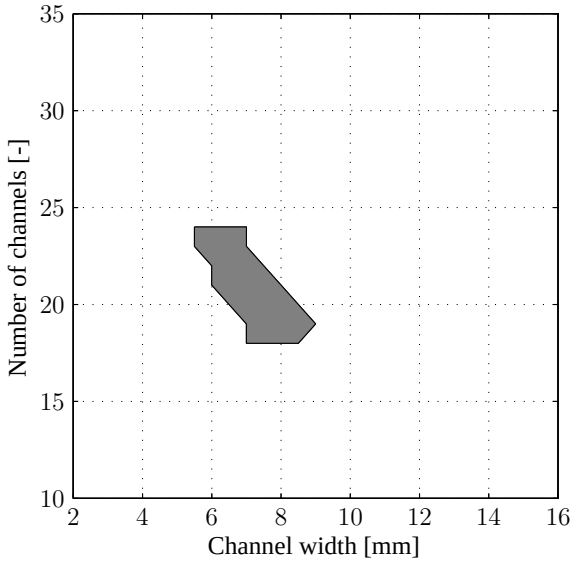

Fig. 3.1: Allowable combinations of the number and width of radial cooling ducts.

3.3 Conclusions

By applying the lumped-parameter-based thermal model, both the steady-state temperatures and transient states were studied. It was discovered that the doubly radial cooling is able to keep the temperature of the stator winding and the rotor surface magnets low enough with

reasonable cooling air flow rates. It was shown that in the doubly radial-cooled DDPMSGs studied, the optimal number of radial cooling ducts is around twenty. That is why the effects of the cooling ducts on the design and performance of the PMSGs should be investigated further.

Chapter 4

Effective stack length of the substacked PMSM

It was shown in the previous chapter that several cooling ducts are needed for the heat transfer of the large-scale DDPMSG using the doubly radial cooling. Typically, the number of axial stator substacks is around twenty and the relative proportion of the cooling ducts of the active length of the machine exceeds 10%. Every radial cooling duct constitutes two additional end areas for the stator substacks. Therefore, it is extremely important to examine the stator stack end effects on the performance of the PMSM. The performance of the PMSG can be considerably improved by compensating the harmful effects of the cooling ducts whenever possible. Also the effect of cooling ducts has to be taken into account when determining the parameters, such as the no-load voltage and inductances, used in the analytical analyses or in the control design of the machine.

When field windings are used, the current linkage is continuous in the axial direction even in the case of cooling ducts. Permanent magnet current linkage, however, stops where the magnet ends. Therefore, if there are any spaces between the permanent magnets in the axial direction, the permanent magnet excitation sees a different effective length compared with a continuous current linkage.

In this chapter, determination of the effective stator stack lengths for permanent magnet and armature coil excitations is studied. The axial cross-section of the machine is studied by the 2D FEM and the air gap flux density integral is analyzed. In the next chapter, the effects determined by the 2D FEM are verified by studying the no-load voltages and the stator synchronous inductances of the machine by the 3D FEM.

4.1 Analytical determination of the effective stack length

Traditionally, the end effects have been taken into account by using the effective length of the machine in the analytical calculations. The effective length means the length of the vir-

tual machine with homogeneous flux density in the axial direction with the same electrical properties, such as the no-load voltage and the torque production capability, as in the studied machine.

The most common way to calculate the effective length of the induction machine is Carter's theory, originally developed to describe the effects of the stator slots in induction machines [58], [59]. In Carter's theory, the physical air gap length of the machine is replaced by the equivalent air gap similarly as the physical length of the machine is replaced by the effective length when the stack end effects are considered. Based on Carter's theory and presented for example in [19], the equivalent length of the machine with radial cooling ducts is

$$l' = l - n\kappa b + 2\delta, \tag{4.1}$$

where l is the total physical length of the machine, n the number of radial cooling ducts, b the physical length of the radial cooling duct, δ the length of the physical air gap, and κ the factor defined as

$$\kappa = \frac{2}{\pi}\left[\arctan\frac{b}{2\delta} - \frac{2\delta}{b}\log\sqrt{1+\left(\frac{b}{2\delta}\right)^2}\right] \approx \frac{\frac{b}{\delta}}{5+\frac{b}{\delta}}. \tag{4.2}$$

From the approximation we can easily see that the factor κ can only have values smaller than one. When κ is smaller than one, according to (4.1) the equivalent length of the machine is always longer than the physical total length of the machine lamination substacks. However, Carter's theory was not developed for permanent magnet machines. The major drawback in the use of Carter's theory on PMSMs is that it does not take into account the permanent magnet leakage flux in the end areas. Instead, Carter's theory is developed for machines with a continuous current linkage produced by the winding reaching beyond the stack and between possible substacks, but the current linkage of the magnets does not exceed the magnet area. The end area leakage flux is also a function of stator geometry, and the rotor magnetic circuits are not taken into account despite the length of the radial cooling ducts and the physical air gap. On the other hand, saturation typically affects the permanent magnet machines, but this is also neglected in Carter's theory.

Because Carter's theory seems not to be suitable to describe the end effects of the permanent magnet machines, the end effects are studied by applying the Finite Element Method. To define the equivalent length of the machine, the cross section of the machine is studied with the 2D FEM, and the integral of the flux along the air gap is examined. A method to implement stack fringing in the 2D by analyzing the cross-section of the machine and then modifying the material properties is described in [60].

4.2 2D analysis of the effective stack length

The effective length of the machine can be studied with the 2D FEM by examining the cross-section of the machine in the axial direction. The effective lengths differ from each other in the case of the rotor and stator magnetizations. In the case of the rotor magnetization, the magnetic flux is produced by the rotor-mounted permanent magnets. The stator magnetization means that the flux is produced by the stator winding, that is, the armature reaction. The stator magnetization can be emulated by setting the remanent flux density of the magnets to zero and adding the magnetization coils around the stator stack. An example of the cross-section described with the 2D FEM of the machine with one radial cooling duct is presented in Fig. 4.1.

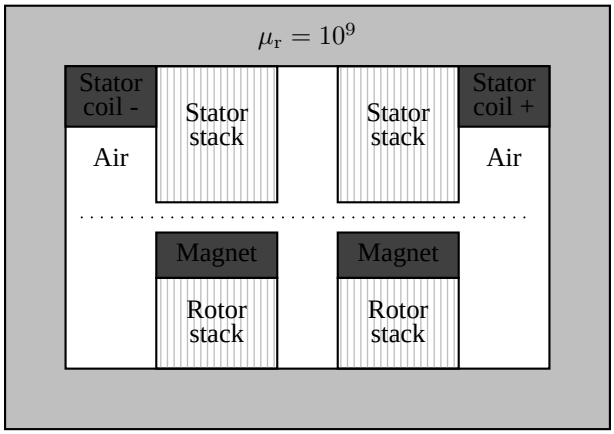

Fig. 4.1: Cross-section of the machine with one radial cooling duct and rotor surface magnets described for the 2D FEM. The stator coils are used in the case of stator magnetization only. This figure is for illustrative purposes alone, for example the air regions around the stacks are wider in the geometry used for calculations to prevent flux leakage from the stack to the surrounding high-permeability yoke.

The lamination stacks of the machine are short circuited with a material having a very high relative permeability $\mu_r = 10^9$ to produce the path for the flux to travel between the stator and rotor circuit. The material of the lamination stacks is described as an anisotropic linear magnetic material. In the axial direction, the flux must travel through the lamination and the non-magnetic insulation between the laminates, which decreases the permeability drastically in the axial direction. If the proportions of the steel and the insulation material are 0.97 and 0.03, respectively, the total relative permeability in the axial direction is

$$\mu_{r,\mathrm{axial}} = \frac{1}{\frac{0.97}{\mu_{r,\mathrm{Fe}}} + \frac{0.03}{\mu_{0,r}}} \approx 33, \tag{4.3}$$

where $\mu_{0,r}$ is the relative permeability of the vacuum that is equal to 1. The relative permeability of the non-saturated steel does not significantly affect the permeability in the axial direction, because with any $\mu_{r,\mathrm{Fe}} > 1300$ $\mu_{r,\mathrm{axial}} \approx 33$, if the proportions of the steel and

the insulation material are as mentioned above. The magnets are described as linear magnets with a constant remanent flux density B_r and a relative permeability $\mu_{\mathrm{r,PM}} = 1.05$.

The equivalent length of the machine is defined by dividing the integral of the flux normal component along the middle line of the air gap in the axial direction shown in Fig. 4.1 by the flux of the homogeneous machine

$$l' = \frac{\int B \mathrm{d}z}{B_\mathrm{homog}}, \tag{4.4}$$

where z is the coordinate in the axial direction. The flux of the infinitely long machine without cooling ducts B_homog can be defined by the FEM by setting boundary conditions at the ends of the machine stack area thereby preventing the leakage flux belly to the end air areas. On the other hand, the effect of the non-saturated iron is quite small on the reluctance of the magnetic circuit. Thus, the air gap flux density for the homogeneous machine can be calculated, neglecting the iron parts, by

$$B_\mathrm{homog} = \frac{h_\mathrm{PM} B_\mathrm{r}}{\mu_{\mathrm{r,PM}}} \frac{1}{\frac{h_\mathrm{PM}}{\mu_{\mathrm{r,PM}}} + \frac{\delta}{1}}, \tag{4.5}$$

where h_PM is the height of the permanent magnet. In the case of the stator magnetization, the current linkage is produced by the armature windings and the air gap flux density for the homogeneous machine is

$$B_\mathrm{homog} = \mu_0 \frac{\Theta}{\frac{h_\mathrm{PM}}{\mu_{\mathrm{r,PM}}} + \frac{\delta}{1}}, \tag{4.6}$$

where Θ is the current linkage of the magnetizing armature coils.

4.3 Results

As presented in Publication IV, the end effects both at the machine ends and at the cooling duct areas decrease the effective length of the machine when rotor permanent magnet excitation is used. This shows that it is impossible to apply Carter's theory to the calculation of the effective length of the PMSM, as (4.1) shows that the effective length must be longer that the sum of the physical lengths of the stacks. The decrease in the effective length is a consequence of the magnet leakage fluxes traveling through the air at the stack ends. The effective length for the permanent magnet excitation of the machine was shorter than the physical length of the stacks for both the machines with rotor-surface-mounted magnets and rotor-buried magnets.

It seems that it is very difficult to formulate a generic equation to determine the effective length of the PMSM. The effect of the end region phenomena depends on the geometry of the magnetic circuit and the magnetic state of the circuit. Thus, there are too many degrees of freedom in the design of the magnetic circuit of a PMSM to be able to fully examine all the related effects and cross-effects.

In the case of the stator magnetization, the equivalent length of the machine is, however, longer than the physical length of the stacks with and without cooling ducts because of the flux fringing in the end areas. For example, with the rotor PM magnetization, the equivalent length of the $60\ \mathrm{mm}$ stack shown in Fig. 5 in Publication IV is less than the physical length of the stack, but with the stator coil magnetization, the effective length, $l' = 75.7\ \mathrm{mm}$, significantly exceeds the physical length of the stack. The flux density normal components in the middle of the air gap with the rotor and stator magnetizations for the geometry examined in Fig. 10 in Publication IV are presented in Fig. 4.2.

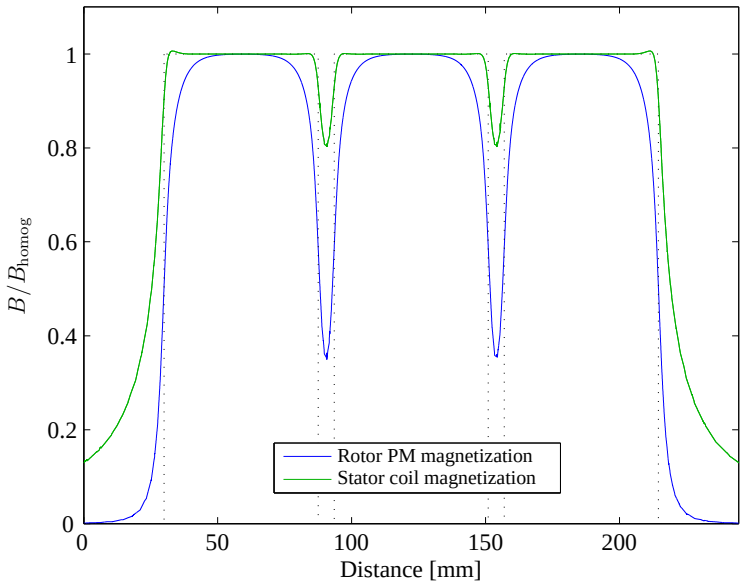

Fig. 4.2: Air gap flux density normal component waveforms in the axial direction with the rotor PM and stator coil magnetizations. The physical stack area is indicated by the black dotted line.

The PM flux leakage near the substack end areas is clearly seen as the flux density is considerably lower than in the middle of the substacks. The flux fringing, increasing the effective length of the machine, in the stack end areas is much more intense in the case of the stator coil magnetization although some flux fringing takes place with the rotor PM magnetization also. Examples of the flux lines of the leakage and fringing flux in the stack end areas are presented in Fig. 4.3.

The effective length of the three $57.5\ \mathrm{mm}$ stacks is $172.3\ \mathrm{mm}$ in the case of the rotor PM magnetization and $205.9\ \mathrm{mm}$ in the case of the stator coil magnetization. In the case of the stator coil magnetization, the approximation for the effective length of the machine with

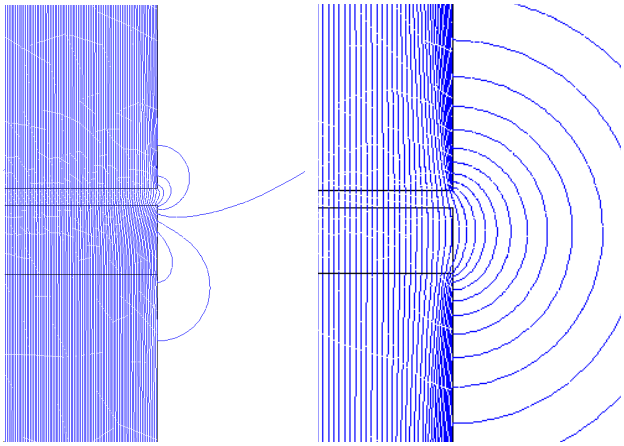

(a) Rotor PM magnetization *(b) Stator coil magnetization*

Fig. 4.3: Flux leakage and fringing in the end areas near the air gap with the rotor surface magnets.

rotor-surface-mounted magnets can be calculated by (4.1) as the magnet height is taken into account in the air gap length. When the modified air gap length is $(5 + 8/\mu_{\mathrm{r,PM}})$ mm, the analytically calculated value is 208.8 mm, and a less than 2% error is made compared with the value calculated by the 2D FEM. For the single 60 mm stack, the analytically calculated equivalent length is 79.4 mm, which is approximately 5% more than with the FEM.

From the machine performance point of view, the decrease in the PM flux is harmful. As the flux and no-load voltage of the machine decrease, more armature current is needed to produce the same power or torque. Consequently, methods to compensate the harmful end effects are needed. In Publication IV, it is proposed that the rotor stack should be designed slightly longer than the stator stack. It was shown that an extension of the rotor stack can usually compensate the flux dissipated into the stack end leakage flux. Again, it was found that it is not possible to give an exact equation for the rotor extension needed to compensate the end effects. It was also found that the extension of the rotor stack ends by the air gap length could be a good initial guess, but the effect of the extension should be verified by the FEM. It must be borne in mind that the extension of the rotor substacks decreases the width of the rotor cooling ducts, and the heat transfer capability of the narrowed rotor cooling ducts has to be ensured. If the doubly radial cooling is used, the rotor ducts can even be totally filled to maximize the air gap flux.

4.4 Conclusions

A method to calculate the effective stack length by the 2D FEM applying the axial cross-section of the machine was introduced. It was shown that the end effects in the stack end and cooling ducts areas significantly decrease the PM flux of the machine. The loss of the PM flux can be compensated by making the rotor stack and magnets longer than the corresponding stator stack.

In the case of the stator magnetization, the equivalent length of the machine exceeds the physical length of the stacks because of the intense flux fringing in the substack end areas. Consequently, the equivalent length is different in the cases of the rotor PM and stator coil magnetizations.

Chapter 5

Effect of substacking on the no-load voltage and synchronous inductances

The effect of radial cooling ducts on the no-load voltage and synchronous inductances of the PMSM were studied by the 3D FEM to verify the effects determined by the 2D analysis of the air gap flux in the previous chapter. For several reasons, the 3D analysis gives more accurate results compared with the 2D analysis. First, the third dimension is described, and the whole machine geometry is present instead of the cross-section. Now, the effects at the stator yoke and the effects of the non-homogeneous air gap length are considered. Further, the lamination model of the Flux3D allows the modeling of the anisotropic non-linear lamination material.

Several different geometries are studied with different combinations of cooling ducts in the stator and the rotor. Two different air gaps are used to change the permeance of the magnetic circuit and thus the flux density to analyze the effects of saturation.

5.1 Geometries studied

To study the end effects of the PMSM by the 3D FEM, a $45\ \mathrm{kW}$ machine with rotor-buried magnets and a nominal speed of $600\ \mathrm{min}^{-1}$ was investigated. More detailed information of the original machine can be found in [61]. The studied machine was chosen instead of the DDPMSG for two reasons. First, there was an actual PMSM of which there were measured no-load voltage data available to verify the 3D FEM model before adding the cooling ducts. The second reason was that the 3D FEM analysis of one segment of the DDPMSG with ten poles and numerous radial cooling ducts would provide no further information of the studied phenomena compared with the selected machine regardless of the drastically increased computational load that would be practically excessive for the present-day desktop computers.

To further decrease the number of elements and the computational load, only one pole of the machine was modeled as shown in Fig. 5.1. Because of the axial symmetry, only one half of the machine was needed in the axial direction.

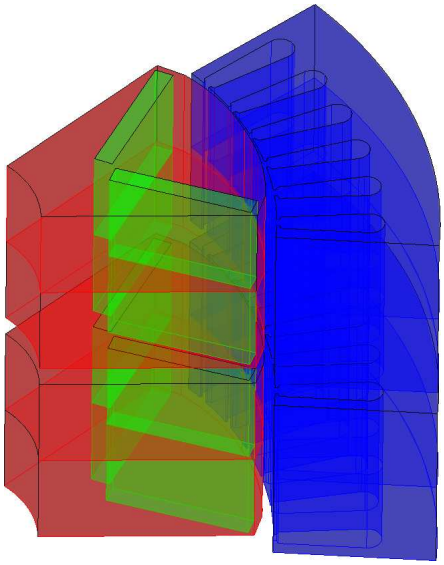

Fig. 5.1: Geometry of the machine without non-meshed coil conductors placed in the stator slots.

The winding of the machine is replaced by the bar-shaped non-meshed coil conductors. The end area winding is imitated by extending the non-meshed conductor beyond the stator stack area. The anisotropic lamination material is described by applying the lamination model of the Flux3D software with the space factor for iron $k_{\mathrm{f}} = 0.98$.

Six different geometries were studied. Three of the geometries have no cooling ducts at all. Two of the geometries have cooling ducts both in the stator and in the rotor, and one of the geometries has cooling ducts in the stator only. The lengths of the substacks and the cooling ducts are presented in Table 5.1. Model A is the original form of the machine without cooling ducts. The stator of Model B equals the stator of Model A, but the rotor is somewhat longer than the rotor of Model A. In Model C, three $10\ \mathrm{mm}$ cooling ducts are added to Model A both in the stator and in the rotor. Model D is equal to Model C, but all the rotor substacks are slightly longer than the stator substacks. Model E has the same stator as Model D, but all the rotor cooling ducts are filled. There is also an additional geometry to investigate the end effects without cooling ducts. The shape of the machine is equal to Model A, but both the stator and rotor stacks are essentially longer. More detailed illustrations of the geometries can be found in Publication V. All the geometries were studied with $1.2\ \mathrm{mm}$ and $5.0\ \mathrm{mm}$ air gaps.

5.2 No-load voltages

The no-load voltages were calculated by rotating the machine at its nominal speed for one period of the voltage after stabilization. All the phases were symmetrical and the voltage

Table 5.1: GEOMETRIES EXPLORED

Rotor stack and cooling channels Stator stack and cooling channels	Geometry
R 280 mm S 280 mm	Model A
R 282.4 mm S 280 mm	Model B
R 300 mm S 300 mm	-
R 4×70 mm $+ 3 \times 10$ mm S 4×70 mm $+ 3 \times 10$ mm	Model C
R 4×72.4 mm $+ 3 \times 7.6$ mm S 4×70 mm $+ 3 \times 10$ mm	Model D
R 312.4 mm S 4×70 mm $+ 3 \times 10$ mm	Model E
2D 280 mm	2D

waveform was sinusoidal. The measured phase voltage RMS value was 353.4 V. As the RMS voltage for Model A with the original 1.2 mm air gap was 354.2 V, it can be assumed that the 3D model corresponds very well with the measured voltage. The 2D FEM overestimates the no-load voltage approximately by 4%, because neither the end effects nor the lamination space factor are taken into account. The no-load voltages with the 1.2 mm air gap are presented in Table 5.2.

Table 5.2: NO-LOAD VOLTAGE RMS VALUES WITH A 1.2 mm AIR GAP

Geometry	E_{PM} (V)
Model A	354.2
Model B	356.2
R 300 mm S 300 mm	380.2
Model C	349.0
Model D	359.0
Model E	374.7
2D	368.2

The effect of the end area phenomena can be estimated by the proportion

$$\frac{l_{280\ \mathrm{mm}} + l_{\mathrm{ends}}}{l_{300\ \mathrm{mm}} + l_{\mathrm{ends}}} = \frac{E_{\mathrm{PM},280\ \mathrm{mm}}}{E_{\mathrm{PM},300\ \mathrm{mm}}}, \tag{5.1}$$

where $l_{x\ \mathrm{mm}}$ is the physical length x of the stack, l_{ends} is the sum of the effective length of the end regions, and $E_{\mathrm{PM},x\ \mathrm{mm}}$ is the no-load voltage with the physical stack length x. By solving and discarding the effective length of the end regions, the machine with 280 mm

stacks should produce 364.3 V no-load voltage, which is quite close to the value calculated by the 2D FEM. It can also be seen that the end area PM flux leakage decreases the no-load voltage approximately by 3%. The air gap length rotor stack extension of Model B increases the no-load voltage a little, but not enough to totally compensate the voltage loss caused by the end area leakage.

The cooling ducts of Model C decrease the no-load voltage approximately by 1.5% compared with Model A with uniform stacks. In this case, lengthening the rotor substacks by the air gap length in Model D is enough to compensate the effect of the cooling ducts by means of the no-load voltage. But still, the no-load voltage is lower than the no-load voltage of the virtual uniform machine without cooling ducts and stack end effects.

If the rotor cooling ducts are totally filled by the rotor stack as in Model E, the no-load voltage is higher than the no-load voltage of the virtual machine without cooling ducts and stack end effects. Because of the saturation in the stator, the no-load voltage of the machine with the uniform rotor and cooling ducts in the stator has a lower no-load voltage than the machine with the 300 mm uniform stator and rotor stacks, although the physical length of the rotor stack and magnets is now more than in Model A.

With the 5.0 mm air gap, the no-load voltages presented in Table 5.3 are all lower than with the 1.2 mm air gap because of the increased reluctance of the magnetic circuit.

Table 5.3: NO-LOAD VOLTAGE RMS VALUES WITH A 5.0 mm AIR GAP

Geometry	E_{PM} (V)
Model A	202.9
Model B	206.5
R 300 mm S 300 mm	217.9
Model C	201.5
Model D	219.9
Model E	222.5
2D	209.9

The results give mainly the same conclusions as with the shorter air gap. In this case, the magnetic circuit is not as close to the saturation as earlier, and the extensions of the substacks are considerably larger. The no-load voltage of the virtual machine with 280 mm homogeneous stacks would produce 209.9 V no-load voltage. The extension of the rotor stack by the air gap length at both ends is not able to totally compensate the PM flux end area leakage in the case of the uniform stacks, but by extending the rotor substacks in the case of three cooling ducts, the effect of cooling ducts on the no-load voltage can be compensated. Because of the lower saturation with the 5.0 mm air gap, the no-load voltage of Model E with a long uniform rotor is higher than the no-load voltage of the machine with 300 mm stacks.

5.3 Inductances

The direct- and quadrature-axis inductances were calculated as a function of current for all of the geometries presented above. The direct- and quadrature-axis current values were varied beyond the nominal current value for both the positive and negative directions. Also the inductances were studied with $1.2\ \mathrm{mm}$ and $5.0\ \mathrm{mm}$ air gaps to determine the effect of saturation.

The studied inductance is the stator total inductance including the magnetization inductance and the leakage inductance of the stator. The inductance is calculated by

$$L_{\mathrm{d/q}} = \frac{\Delta\psi_{\mathrm{d/q}} N_{\mathrm{ph}}}{\Delta\Theta_{\mathrm{sd/q}}} = \frac{\Delta\psi_{\mathrm{d/q}}}{\Delta i_{\mathrm{sd/q}}} = \frac{2\Delta\phi_{\mathrm{d/q}}}{\Delta i_{\mathrm{sd/q}}}, \tag{5.2}$$

where $\psi_{\mathrm{d/q}}$ is the flux linkage of the coil, $\Theta_{\mathrm{sd/q}}$ the direct-/quadrature-axis coil current linkage, N_{ph} the number of series-connected coil turns, $\phi_{\mathrm{d/q}}$ the flux linkage seen by one coil side, and $i_{\mathrm{sd/q}}$ the direct-/quadrature-axis current component of one coil turn.

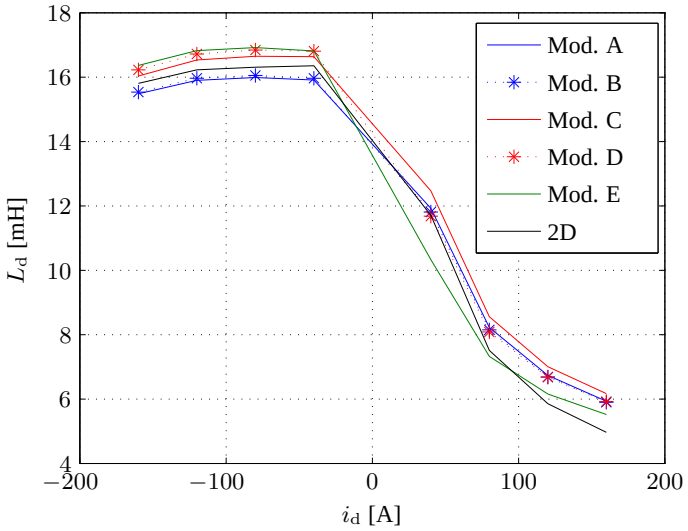

Fig. 5.2: Direct-axis total inductance with a $1.2\ \mathrm{mm}$ *air gap.*

The direct-axis inductances as a function of stator current are shown in Fig. 5.2. It can be seen that the direct-axis inductances are almost constant in the demagnetization. The inductance of Model E is highest because of the longest rotor stacks. The extension of the rotor increases the inductances regardless of whether there are cooling ducts in the machine or not. The difference compared with the no-load calculations is that the cooling ducts increase the inductance, as they decreased the no-load voltage. The increase in the inductance is

probably explained by the increase in the stator flux leakage and the stator flux fringing. Part of the leakage flux travels through the substack laminates decreasing the reluctance of the leakage flux path. The flux paths in the stack end regions are described in [62]. The 2D cross-section simulations with the stator magnetization indicated an increase in the armature-produced air gap flux as a consequence of the cooling ducts, which refers to an increase in the magnetization inductance. However, with the 3D, the integration of the air gap flux contained too much inaccuracy to determine the magnetization inductance separately by integrating the air gap flux density.

The inductance calculated by the 2D is higher than the inductance of Models A and B because of the higher space factor of the stacks. On the other hand, the 2D inductance is lower than the inductance of Models C, D, and E because the effect of the cooling ducts is not taken into account. Because the inductance is increased as the cooling ducts are added, it can be said that in the case of stator magnetization the effective length of the machine is increased because of the cooling ducts.

In the positive current region, the significant decrease in the inductances can be seen as a result of saturation. The most interesting observation is that Models D and E saturate most drastically. This is probably explained by the high saturation of the stator teeth in the areas near the rotor stack extensions. Because of the insulation between laminates, the flux cannot easily move from a laminate sheet to another, leading to heavy saturation of the outermost lamination sheets. With a longer air gap, the phenomena remain the same, but the saturation shifts to the higher stator currents.

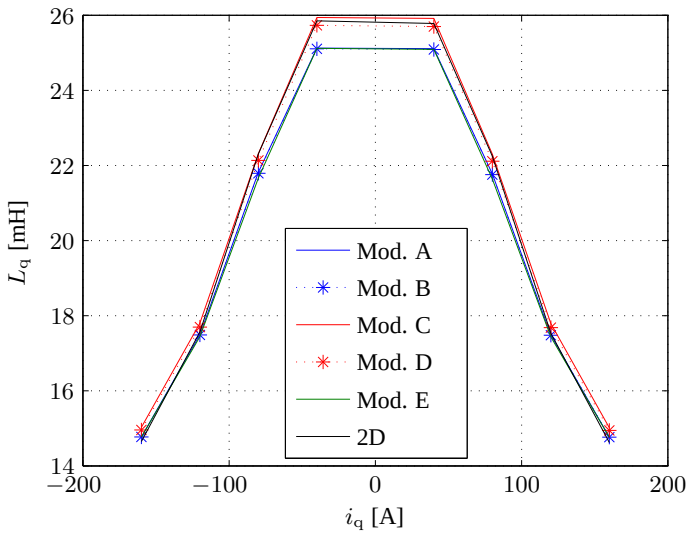

Fig. 5.3: Quadrature-axis total inductance with a $1.2\ \mathrm{mm}$ *air gap.*

The quadrature-axis inductances presented in Fig. 5.3 are not dependent on the sign of the current because the magnets do not produce flux in the quadrature-axis direction. Surprisingly,

the inductance of the machine with uniform rotor and cooling ducts in the stator has the lowest quadrature-axis inductance. The inductance of Model C is higher than the inductance of Model D where the rotor stacks are extended. The explanation must be the cross-saturation between the permanent magnets in the direct-axis direction and the quadrature-axis inductances. The higher flux density in the direct-axis direction saturates the magnetic circuit at the stator teeth when the rotor extensions are used, and thus, the quadrature-axis inductance decreases.

5.4 Conclusions

It was found that the cooling ducts and the stack end area effects have a significant effect on the machine no-load voltage and inductances. The end effects and the cooling ducts decrease the permanent magnet flux, and thereby the no-load voltage, and consequently, the effective length of the machine. Thus, the traditional 2D FEM calculation easily overestimates the no-load voltage of the machine.

With the 2D FEM, the inductances are typically overestimated for the machine without cooling ducts because the stacking factor of the lamination stack is typically neglected. In the case of several cooling ducts, the inductances are underestimated with the 2D FEM because the increase in the stator flux leakage and fringing in the cooling duct areas are not taken into account.

The loss of the no-load voltage in the case of several cooling ducts can be compensated by making the rotor substacks slightly longer than the corresponding stator substack. If the rotor stacks are extended too much, the stator teeth laminates easily saturate heavily in the vicinity of the cooling duct. The optimal extension must be found by trial and error, but the air gap length is a good initial guess.

It was found that the end area effects and the cooling ducts decrease the no-load voltage, but increase the inductances. That is why different effective stack lengths should be used when determining the no-load voltage and the inductances with the 2D FEM for a PMSM. The decreased voltage and increased inductances reduce the torque production capability of the machine. The increased inductances can easily cause the saturation of the stator circuit at higher loads with an intense armature reaction, if the flux increase caused by the armature reaction is not compensated by the control.

On the other hand, the effective length of the machine when calculating the performance of the machine at load should be somewhere between the effective lengths determined for the no-load voltage and inductance calculations. In the future, the problem can be easily solved when the computation power increases so much that it is possible to study the machine under load with the 3D FEM.

Chapter 6

Determining the efficiency of the PMSGs analytically including saturation

The no-load voltages and inductances determined in the previous chapter can be used in the analytical calculation and control design of the PMSGs. In Publication VI, the efficiencies of several PMSMs are calculated applying four different control strategies over the whole speed and torque ranges of the machines. The studied machines are a DDPMSG, a salient-pole PMSG, and a PMSM for hybrid drive applications. In this chapter, also the effect of inductance saturation on the efficiency of the PMSMs is studied by comparing the efficiencies of the $45\ \mathrm{kW}$ machine described in the previous chapter with and without saturating inductances.

By the definition of the electromagnetic torque, based on the Lorentz force as a cross product of the flux and the current, the torque equation for a permanent magnet machine is

$$T = \frac{3p}{2}|\vec{\psi}_\mathrm{s} \times \vec{i}_\mathrm{s}| = \frac{3p}{2}(\psi_\mathrm{d} i_\mathrm{q} - \psi_\mathrm{q} i_\mathrm{d}). \tag{6.1}$$

When the flux linkage components ψ_d and ψ_q are replaced with currents and synchronous inductances, the torque equation can be written in a more simple form

$$T = \frac{3p}{2}\left[(L_\mathrm{d} - L_\mathrm{q}) i_\mathrm{d} i_\mathrm{q} + \psi_\mathrm{PM} i_\mathrm{q}\right]. \tag{6.2}$$

To produce the desired torque, a definite combination of the currents i_d and i_q must be found. At the same time, the current combination must meet the requirements of the desired control principle.

6.1 Control methods

Various control methods for the PMSMs are introduced in the literature. The traditional control methods are based on different principles of the selection of the load angle. The torque production capability as a function of current of $\cos\phi = 1$ control and the maximum torque per ampere control are compared with each other in [63]. The torque production capabilities and the power factors of the $i_\mathrm{d} = 0$ control, $\cos\phi = 1$ control, linear torque control, and the constant flux linkage control are compared as a function of current in [64]. Torques, power factors, and stator voltages of the $i_\mathrm{d} = 0$ control, $\cos\phi = 1$ control, and the constant flux linkage control are compared as a function of current in [65]. In [66], a method to minimize the losses of the PMSM is introduced. The leakage inductances are neglected and the iron losses are implemented using the constant iron loss resistance. The effect of the machine parameters on the machine control is studied, and a method to minimize the stator current by on-line control of the stator flux linkage reference in the case of the direct torque control is introduced in [67]. Next, the control methods studied in Publication VI are introduced in brief.

6.1.1 $i_\mathrm{d} = 0$ control

In the $i_\mathrm{d} = 0$ control, the direct-axis current is set to zero, and hence, the stator flux linkage is determined by the permanent magnet flux linkage and torque of the machine. In non-salient pole machines, the direct-axis current does not produce torque, and therefore, the $i_\mathrm{d} = 0$ control minimizes the copper losses of the non-salient pole machines. The use of the $i_\mathrm{d} = 0$ control is typically limited because the voltage increase caused by the armature reaction cannot be compensated as shown in Fig. 6.1.

Not only the voltage increases as the torque increases, but also the power factor of the machine decreases substantially at high loads because the phase angle is equal to the load angle in the case of the $i_\mathrm{d} = 0$ control. The $i_\mathrm{d} = 0$ control is best suited for non-salient pole machines with low inductances.

6.1.2 $\cos\phi = 1$ control

In the $\cos\phi = 1$ control, the power factor is kept equal to one. This means that the stator current and stator voltage vectors are pointing in the same direction, and the machine is neither producing nor consuming reactive power, and the apparent power is minimized. Typically, the $\cos\phi = 1$ control requires demagnetizing current to at least partially compensate the armature reaction and to decrease the stator voltage amplitude. A proportionality equation for the stator current and voltage components is

$$\frac{u_\mathrm{d}}{u_\mathrm{q}} = \frac{i_\mathrm{d}}{i_\mathrm{q}} = \frac{R_\mathrm{s} i_\mathrm{d} - \omega\psi_\mathrm{q}}{R_\mathrm{s} i_\mathrm{q} + \omega\psi_\mathrm{d}}, \tag{6.3}$$

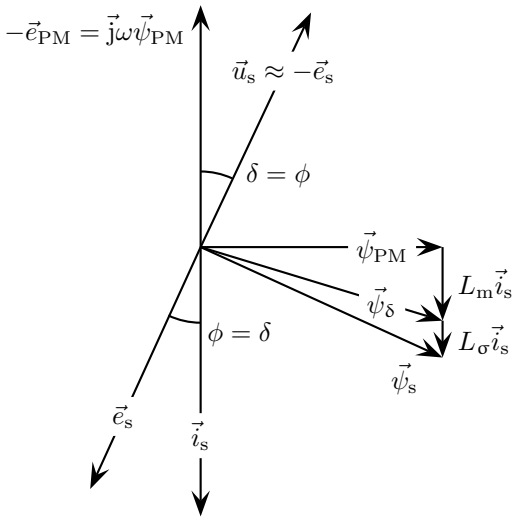

Fig. 6.1: Phasor diagram of the direct-driven wind generator at nominal speed and torque.

where u_{d} and u_{q} are the direct- and quadrature-axis stator voltage components and R_{s} is the stator resistance. When the quadrature-axis current i_{q} is known, the direct-axis current i_{d} is derived by (6.3). The equation of the i_{d} current in the $\cos\phi = 1$ control is

$$i_{\mathrm{d}} = \frac{-\psi_{\mathrm{PM}} \pm \sqrt{\psi_{\mathrm{PM}}^2 - 4L_{\mathrm{d}}L_{\mathrm{q}}i_{\mathrm{q}}^2}}{2L_{\mathrm{d}}}, \tag{6.4}$$

where $L_{\mathrm{d}} = L_{\mathrm{md}} + L_{\sigma}$ and $L_{\mathrm{q}} = L_{\mathrm{mq}} + L_{\sigma}$ are the direct- and quadrature-axis synchronous inductances, respectively.

The $\cos\phi = 1$ control can be used if the radicand in (6.4) is positive. The root is positive if the inductances L_{d}, L_{q}, and the current i_{q} that depend on the torque are small enough and the permanent magnet flux linkage ψ_{PM} is large enough.

6.1.3 i_{s}=minimum control

The implementation of this control method that minimizes the stator current is presented in [68]. Contrary to the $i_{\mathrm{d}} = 0$ control, the i_{s}=minimum control allows the use of the reluctance torque by exploiting the direct-axis current in the case of the salient pole machines. In this method, the normalized values of the torque and the direct- and quadrature-axis currents are used

$$T_{\mathrm{n}} = \frac{T}{T_{\mathrm{b}}},\ i_{\mathrm{q,n}} = \frac{i_{\mathrm{q}}}{i_{\mathrm{b}}},\ i_{\mathrm{d,n}} = \frac{i_{\mathrm{d}}}{i_{\mathrm{b}}}, \tag{6.5}$$

where

$$T_{\mathrm{b}} = \frac{3}{2} p \psi_{\mathrm{PM}} i_{\mathrm{b}},\ i_{\mathrm{b}} = \frac{\psi_{\mathrm{PM}}}{L_{\mathrm{q}} - L_{\mathrm{d}}}. \tag{6.6}$$

All motor parameters are eliminated from the normalized torque and currents. As seen from the denominator of the current base value, the current minimization is valid for the salient pole machines only. The references of the i_{d} and i_{q} currents that minimize the stator current are a solution of

$$|T_{\mathrm{nref}}| = \sqrt{i_{\mathrm{d,nref}} \left(i_{\mathrm{d,nref}} - 1\right)^3}, \tag{6.7}$$

$$T_{\mathrm{nref}} = \frac{i_{\mathrm{q,nref}}}{2} \left(1 + \sqrt{1 + 4 i_{\mathrm{q,nref}}^2}\right). \tag{6.8}$$

The references of the currents i_{d} and i_{q} are independent of each other and determined by the torque reference value alone. The current values are minimized based on the saliency of the machine, and the effects of the iron losses are neglected.

6.1.4 u_{s} = optimum control

This is not an actual control method, but the stator voltage is iterated to find the highest efficiency. The stator current is determined from the stator voltage

$$\begin{aligned} u_{\mathrm{s}}^2 &= u_{\mathrm{d}}^2 + u_{\mathrm{q}}^2 \\ &= (R_{\mathrm{s}} i_{\mathrm{d}} - \omega \psi_{\mathrm{q}})^2 + (R_{\mathrm{s}} i_{\mathrm{q}} + \omega \psi_{\mathrm{d}})^2. \end{aligned} \tag{6.9}$$

The direct-axis current can be determined by

$$\begin{aligned} i_{\mathrm{d}} = & \frac{1}{2(R_{\mathrm{s}}^2 + \omega^2 L_{\mathrm{d}}^2)} \times \Bigg(-2\omega^2 L_{\mathrm{d}} \psi_{\mathrm{PM}} - 2 R_{\mathrm{s}} \omega i_{\mathrm{q}} \Delta L \pm \\ & \sqrt{\left(2\omega^2 L_{\mathrm{d}} \psi_{\mathrm{PM}} + 2 R_{\mathrm{s}} \omega i_{\mathrm{q}} \Delta L\right)^2 - 4(R_{\mathrm{s}}^2 + \omega^2 L_{\mathrm{d}}^2) \times} \\ & \overline{\left(\omega^2 \psi_{\mathrm{PM}}^2 + (R_{\mathrm{s}}^2 + \omega^2 L_{\mathrm{q}}^2) i_{\mathrm{q}}^2 + 2\omega R_{\mathrm{s}} \psi_{\mathrm{PM}} i_{\mathrm{q}} - u_{\mathrm{s}}^2\right)} \Bigg), \end{aligned} \tag{6.10}$$

where $\Delta L = L_{\mathrm{d}} - L_{\mathrm{q}}$. As it can be seen in (6.10) the direct-axis current depends on the quadrature-axis current i_{q}, the frequency, and the stator voltage. At rotation speeds higher

than the nominal speed, the stator voltage rises above the nominal voltage, which means that stator flux weakening must be used. Usually, the stator voltage must be constrained to match the inverter voltage limit. In this control method, the direct-axis current i_d, the quadrature-axis current i_q, and the power factor $\cos\phi$ are determined based on torque, rotation speed, and stator voltage.

6.2 Control comparison

The efficiencies were calculated for three test machines including one DDPMSG with all the control methods over the whole speed and torque range. Iteration was needed to solve the current components for the salient pole machines. The iteration process is described as a flow chart in Publication VI.

For the non-salient pole DDPMSG the current minimization, $u_\mathrm{s}=$optimum, and $i_\mathrm{d}=0$ controls all give the same results because the $i_\mathrm{d}=0$ control obviously minimizes the copper losses of the non-salient pole machine. The $\cos\phi=1$ control gives significantly lower performance for the machine. It is clearly seen that the voltage of the $i_\mathrm{d}=0$ control is higher than the nominal voltage at higher loads. Because the iron losses of the DDPMSG are neglected as a result of the low frequency, the efficiency of the DDPMSG decreases as the torque and current increase. As the armature reaction increases at higher torques, also the power factor of the DDPMSG decreases.

In Publication VI, the iron losses were neglected in the case of the non-salient pole DDPMSG. To illustrate the effect of iron losses, the iron loss of the nominal point calculated by the FEM was scaled to the whole speed and torque range, because the analytical calculation of the iron losses may contain significant inaccuracy. It was assumed that the iron loss depends on the voltage and the frequency $P_\mathrm{Fe} \propto \left(U_\mathrm{s}/U_\mathrm{s,n}\right)^2 \left(f/f_\mathrm{n}\right)^{\frac{3}{2}}$ although the iron loss in the demagnetization zone can be underestimated. The efficiency of the DDPMSG with and without iron losses with the $u_\mathrm{s}=$optimum and $i_\mathrm{d}=0$ controls is presented in Fig. 6.2.

When iron losses are not taken into account, the $u_\mathrm{s}=$optimum and $i_\mathrm{d}=0$ controls both minimize the current and yield the same efficiency. When iron losses are taken into account, the $u_\mathrm{s}=$optimum control gives a slightly better efficiency at speeds above the nominal speed where the flux weakening is used to decrease the stator voltage. The optimal stator voltages with and without iron losses are presented in Fig. 6.3.

The optimal voltage is slightly lower when the iron losses are taken into account compared with the case where the iron losses are neglected. Especially in areas above the nominal speed and below the nominal torque, demagnetizing current is used to decrease the stator voltage and iron losses of the machine. Even taking into account the iron losses, the voltage of the nominal operating point is significantly higher than the nominal voltage, which was observed also in Publication VI.

In Publication VI, it is shown that for a salient pole wind generator operating at a higher speed than the DDPMSG studied above, the $u_\mathrm{s}=$optimum and the current minimization give

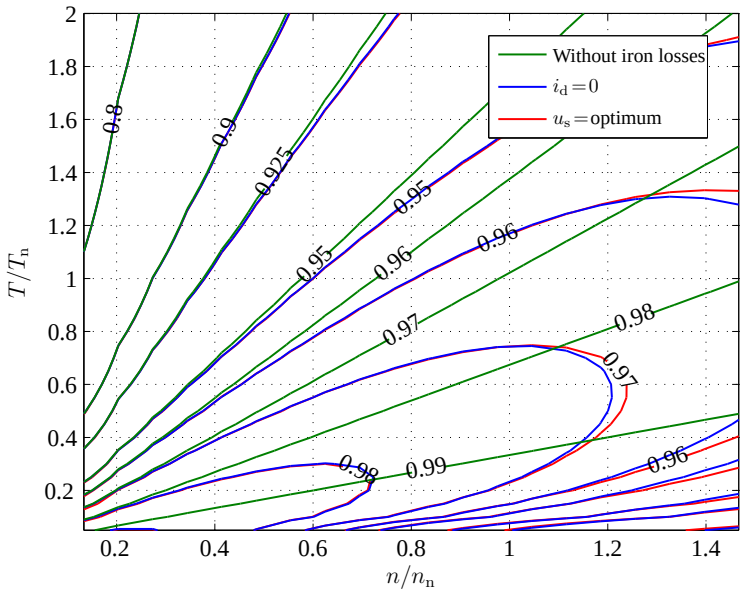

Fig. 6.2: Efficiency of the DDPMSG with and without iron losses. The green lines indicate the efficiency with iron losses with both the $u_\mathrm{s}=$optimum and $i_\mathrm{d}=0$ controls. The blue lines represent the $i_\mathrm{d}=0$ control with iron losses and the red lines the $u_\mathrm{s}=$optimum control with iron losses.

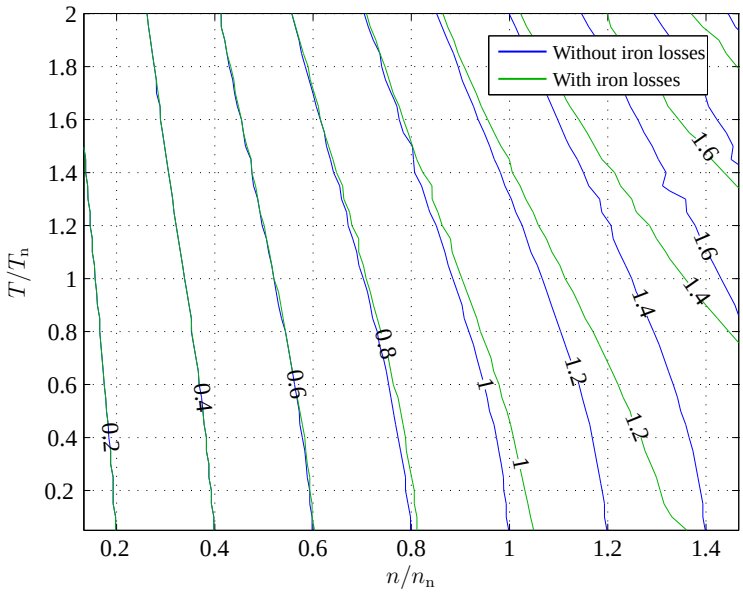

Fig. 6.3: Optimal stator voltage of the DDPMSG with (green) and without (blue) iron losses.

a slightly better performance than the $i_\mathrm{d} = 0$ control. Because the iron losses are now taken into account, the best performance is not achieved at very small torques as in the case of the DDPMSG without iron losses. It was found that the $\cos\phi = 1$ control cannot be used for the PMSG with negative saliency at torques higher than approximately half the nominal torque. At the nominal operating point, the highest efficiency was reached with a voltage approximately 1.5 times the nominal voltage. Although there is a demagnetizing current to utilize the reluctance torque, the armature reaction is not totally compensated to reach the best performance.

6.3 Effect of inductance saturation

The assumption of constant inductances gives inaccurate results with higher loads, where the armature reaction is significant. To investigate the effect of inductance saturation, the same efficiency calculations were repeated with constant inductances, saturating inductances, and cross-saturating inductances. The cross-saturation means that the effects in the direct-axis direction affect the inductance of the quadrature axis and vice versa. In this case, saturating inductances mean that the inductance saturation is taken into account separately in the cases of the direct- and quadrature-axis and cross-saturation despite the fact that the effect of permanent magnets is neglected. The inductance values were calculated by the FEM and imported into the analytical model. Actually, the imported values for the direct-axis are the flux linkages because the interpolation of the inductance containing discontinuities where the current changes its sign is impossible and the flux linkage includes also the change in the PM flux caused by saturation.

The machine studied is a $45\ \mathrm{kW}$ PMSM used in the 3D calculations. The $45\ \mathrm{kW}$ machine was chosen instead of the DDPMSG to determine the effects of saliency caused by the rotor-buried magnets. The iron losses are calculated for the nominal operating point by the 2D FEM, applying Bertotti's equations, and scaled to all the other operating points as a function of frequency. The inductance values around the current plane are presented in Figs. 6.4 and 6.5.

The efficiencies with different inductances applying the $u_\mathrm{s} =$ optimum control are presented in Fig. 6.6. We can see that the efficiency of the saturated machine is lower at higher torques, where the currents and especially the quadrature-axis current are high, than the efficiency of the non-saturated machine. The lower efficiency is explained by the decreased absolute value of the inductance difference $L_\mathrm{d} - L_\mathrm{q}$ producing the reluctance torque as seen in (6.2). The decrease in the inductance difference results from the higher saturation of the quadrature-axis inductance as the increase in torque mainly increases the quadrature-axis current. The efficiency taking into account the cross-saturation is lowest because the significantly increased quadrature-axis current cross-saturates the path of the PM flux decreasing the direct-axis magnetizing inductance and the PM flux. The absolute value of the inductance difference also decreases because the quadrature-axis inductance, which has a higher non-saturated value in the machines with rotor-buried magnets, saturates more heavily than the direct-axis inductance.

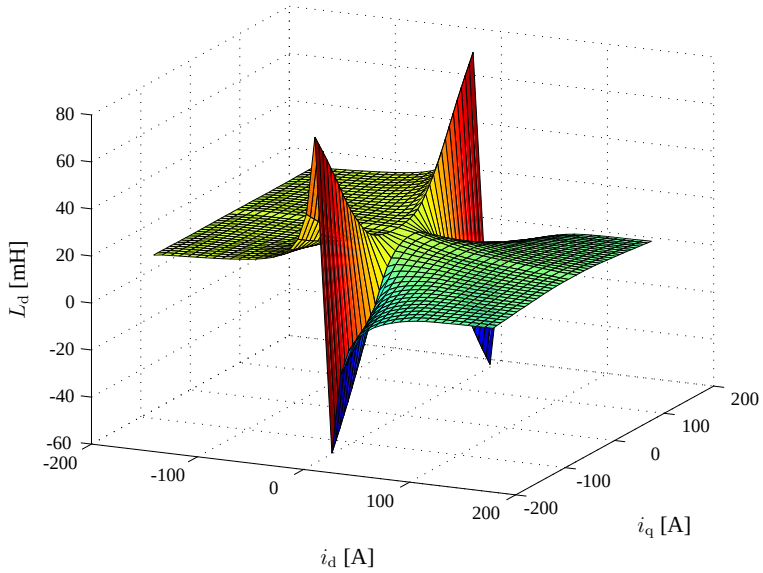

Fig. 6.4: Direct-axis stator inductance as a function of currents.

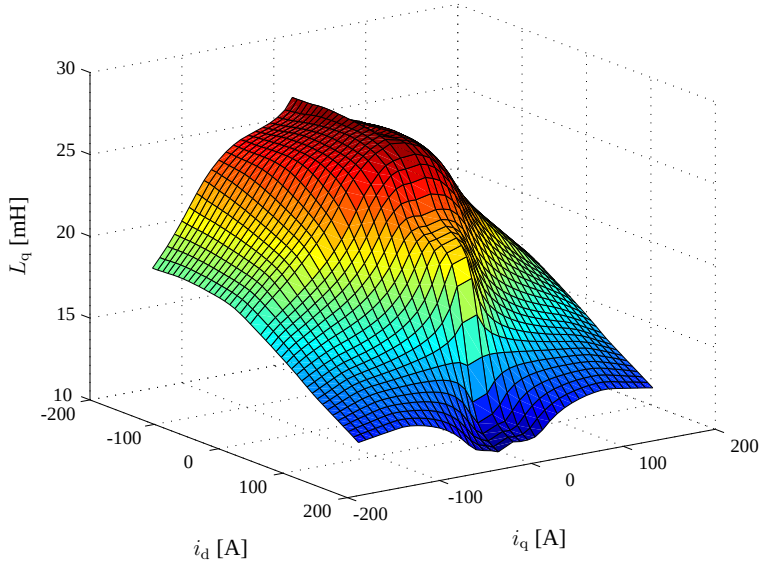

Fig. 6.5: Quadrature-axis stator inductance as a function of currents.

6.4 Conclusions

An analytical model to determine the efficiency of the PMSM at any operating point was developed. Several control methods were compared with each other. It was found that the $i_\mathrm{d} = 0$ control gives the best efficiency for the non-salient pole DDPMSG. When applying

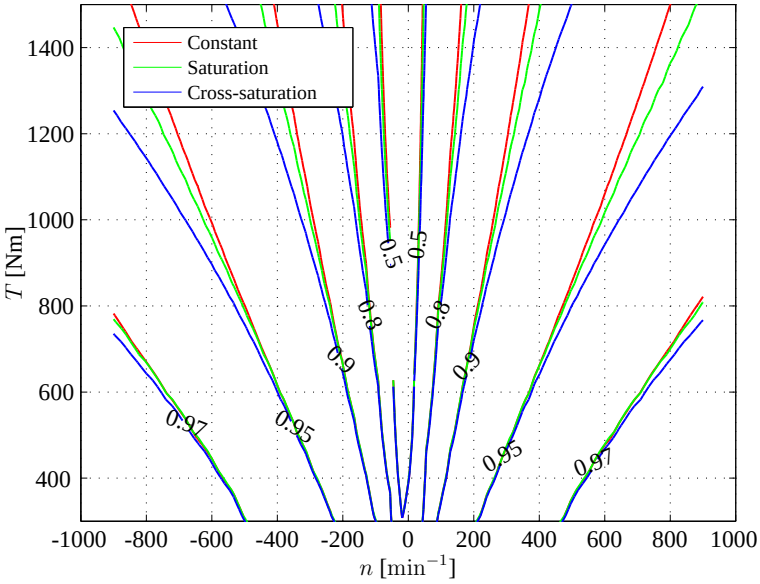

Fig. 6.6: Efficiency of the machine with different inductances.

the $i_\mathrm{d} = 0$ control, the armature reaction significantly increases the stator flux and the voltage at higher loads.

The effect of inductance saturation on the efficiency of the PMSM was studied. The saturation changes the torque production capability of the machine at higher loads as the inductance ratio of the machine changes and the proportion of the leakage flux increases as the main flux path saturates.

Both the $i_\mathrm{d} = 0$ control and the radial cooling ducts of the machine, by increasing the inductances, lead to a strong armature reaction easily causing saturation in the magnetic circuit. Because the saturation was found harmful to the machine efficiency, the powerful armature reaction should be taken into account in the magnetic circuit design process to avoid excessive saturation and performance loss.

Chapter 7

Conclusions and future work

In this doctoral thesis, the special aspects of designing megawatt-range direct-driven permanent magnet synchronous generators for wind turbine applications were discussed. Special attention was paid to the torque quality and the effect of the radial cooling ducts on the electromagnetic performance of the machine.

7.1 Torque quality

The low rotational speed and the high torque set high requirements for the torque quality of the DDPMSG. Several methods to reduce torque ripple were studied. Magnet skew is able to multiply the cogging torque frequency and decrease the amplitude of the cogging torque to a fraction of the initial value. The load torque amplitude is also decreased with skew. Although some of the no-load voltage is lost, the skew should be applied whenever possible.

Magnet shaping reduces both the cogging and the load torque ripple significantly. The best torque quality for the machine with the rotor-surface-mounted magnets was achieved with shaped magnets applying skew. Burying the magnets inside the rotor lamination material makes it possible to modify the air gap flux density distribution by lamination shaping. With rotor-buried magnets, very good torque quality can be achieved, but the rotor leakage flux and the rotor mass increase significantly.

If it is not possible to use skew, it can be imitated by producing asymmetry either in the rotor or in the stator. In the large, segmented stator DDPMSG, the rotor asymmetry with half-filled slots at the edges of the stator segments produces subharmonic load torque ripple components, which are typically not tolerated. By utilizing the stator asymmetry, both the cogging and the load torque ripple amplitudes can be reduced, but low-order harmonics are induced to the load torque.

7.2 Effect of cooling ducts on the machine performance

The temperature distribution of the doubly radially cooled DDPMSG was observed with a thermal resistance network model both in the steady state and during the transient states. The doubly radial cooling was found effective to keep the temperature of the magnets low enough. The number and width of the radial cooling ducts needed were investigated based on the temperature distribution of the machine, the cooling air flow rates in the cooling duct areas and the copper losses of the machine. In multi-megawatt DDPMSGs, numerous radial cooling ducts are needed, which essentially increases the effect of the stack end effects.

The effects of the stack end area fringing on the effective stack length of the PMSM with several cooling ducts were determined by studying the 2D cross-section of the machine in the case of permanent magnet magnetization. Carter's theory was found not suitable for the PM magnetization, because typically the end effects reduce the PM flux of the machine. The effect of stack ends can be compensated by making the rotor stacks and the magnets slightly longer than the stator stacks. In the case of the doubly radial cooling, the rotor stack can be made even uniform if the stator magnetic circuit is designed to avoid saturation.

The results obtained by studying the cross-section of the machine by the 2D FEM were verified by calculating by the 3D FEM the no-load voltages of a PMSM with several different cooling duct geometries. The voltage loss caused by the cooling ducts was defined and the compensation by extending the rotor stack was found beneficial.

To study the effects under stator magnetization, the inductances of the PMSM with several different cooling duct geometries were analyzed as a function of current. The radial cooling ducts increase the stator inductance of the PMSM because of the increased flux fringing and the stator leakage flux in the cooling duct areas. The stator stack lamination easily saturates heavily near the cooling ducts because of the increased leakage flux. It was found that the inductance of the machine without cooling ducts is typically overestimated with the 2D FEM, and the inductance of the machine with several cooling ducts is underestimated. The effective length of the machine is different in the cases of the rotor permanent magnet and stator coil magnetizations.

The different control methods for DDPMSGs were compared with each other. The $i_\mathrm{d} = 0$ control gives the best efficiency for the non-salient pole machines with negligible iron losses, but the voltage rise caused by the anchor reaction at the higher load must be taken into account. The cross-saturation of the magnetic circuit and the inductances decreases the efficiency of the machine at high loads. Because the preferred $i_\mathrm{d} = 0$ control and the radial cooling ducts of the machine strengthen the armature reaction effects by saturating the magnetic circuit, the strong armature reaction should be taken into account during the machine design process to maximize the machine performance.

7.3 Suggestions for the future work

It would be interesting to study the methods to reduce the torque ripple by analyzing a small-scale prototype machine. In particular, it could be useful to experimentally detect the subharmonic torque ripple components caused by the asymmetries.

Furthermore, the effect of the cooling ducts on the PM flux and inductances of the machine could be verified by a prototype machine. An option to apply several different combinations of rotor and stator substack lengths would be required to demonstrate the effect of different cooling duct structures.

It was found that the strengthened armature reaction should be taken into account when designing the magnetic circuit of the machine with several radial cooling ducts to avoid saturation. The optimal dimensioning of the magnetic circuit to maximize the PM flux and avoid saturation without excessive use of lamination material should be studied in more detail.

References

[1] Renewable Energy Policy Network for the 21st Century, "Renewables 2010, global status report," Online: http://bit.ly/GSR2010, Accessed 1 Dec. 2011.

[2] Global Wind Energy Council, "Global wind report 2010," Online: www.gwec.net/index.php?id=180, Accessed 1 Dec. 2011.

[3] Enercon, "Enercon E-126/7.5 MW web site," Online: www.enercon.de/en-en/66.htm, Accessed 1 Dec. 2011.

[4] H. Li and Z. Chen, "Overview of different wind generator systems and their comparisons," *IET Renewable Power Generation*, vol. 2, no. 2, pp. 123–138, Jun. 2008.

[5] L. Hansen, L. Helle, F. Blaabjerg, E. Ritchie, S. Munk-Nielsen, H. Bindner, P. Sørensen, and B. Bak-Jensen, "Conceptual survey of generators and power electronics for wind turbines," *Tech. Rep. Risø-R-1205(EN)*, Risø National Laboratory, Roskilde, Denmark, Dec. 2001.

[6] UpWind, "Concept report on generator topologies, mechanical & electromagnetic optimization," Online: www.upwind.eu/media/811/Deliverable_1B2.b.1.pdf, Accessed 1 Dec. 2011.

[7] A. Hansen and L. Hansen, "Wind turbine concept market penetration over 10 years (1995-2004)," *Wind Energy*, vol. 10, no. 1, pp. 81–97, Jan./Feb. 2007.

[8] J. Slootweg, H. Polinder, and W. Kling, "Dynamic modelling of a wind turbine with doubly fed induction generator," in *Proc. of the IEEE Power Engineering Society Summer Meeting, PES 2001*, Vancouver, Canada, Jul. 2001.

[9] E. Spooner, A. Williamson, and G. Catto, "Modular design of permanent-magnet generators for wind turbines," *IEE Proc. Electric Power Applications*, vol. 143, no. 5, pp. 388–395, Sep. 1996.

[10] H. Polinder, F. van der Pijl, G.-J. de Vilder, and P. Tavner, "Comparison of direct-drive and geared generator concepts for wind turbines," *IEEE Transactions on Energy Conversion*, vol. 21, no. 3, pp. 725–733, Sep. 2006.

[11] J. Cotrell, "A preliminary evaluation of a multiple-generator drivetrain configuration for wind turbines," in *Proc. of the American Society of Mechanical Engineers (ASME) Wind Energy Symposium, WIND 2002*, Reno, USA, Jan. 2002.

[12] Repower, "Repower wind turbines web site," Online: www.repower.de/produkte/windenergieanlagen/?L=1, Accessed 1 Dec. 2011.

[13] J. Manwell, J. McGowan, and A. Rogers, *Wind Energy Explained - Theory, Design and Application*, 1st ed. Chichester, UK: John Wiley & Sons Ltd., 2002.

[14] The Ministry of Employment and the Economy, "Finnish wind atlas," Online: www.tuuliatlas.fi, Accessed 1 Dec. 2011.

[15] R. Tiainen, "Utilization of a time domain simulator in the technical and economic analysis of a wind turbine electric drive train," Doctoral dissertation, Lappeenranta University of Technology, Lappeenranta, Finland, Aug. 2010, Online: http://urn.fi/URN:ISBN:978-952-214-948-0.

[16] W. Cao, X. Huang, I. French, and B. Lu, "Simulation of a site-specific doubly-fed induction generator (DFIG) for wind turbine applications," in *Proc. of the 18th International Conference on Electrical Machines, ICEM 2008*, Vilamoura, Portugal, Sep. 2008.

[17] The Switch, "The Switch wind generators web site," Online: www.theswitch.com/products/wind-power-2/tailored-generators/low-speed-pmgs-3/, Accessed 1 Dec. 2011.

[18] C. Carpenter, "Surface-integral methods of calculating forces on magnetized iron parts," *Proc. of the IEE - Part C: Monographs*, vol. 107, no. 11, pp. 19–28, Mar. 1960.

[19] J. Pyrhönen, T. Jokinen, and V. Hrabovcová, *Design of Rotating Electrical Machines*, 1st ed. Chichester, UK: John Wiley & Sons Ltd., 2008.

[20] C. Versteegh, "Design of the Zephyros Z72 wind turbine with emphasis on the direct drive PM generator," in *Proc. of the Nordic Workshop on Power and Industrial Electronics, NORPIE 2004*, Trondheim, Norway, Jun. 2004.

[21] ABB, "ABB wind generators web site," Online: www.abb.com/product/seitp322/d7a2c5f447b57fbac1256ddb00489a36.aspx?productLanguage=us&country=00, Accessed 1 Dec. 2011.

[22] Siemens, "Siemens wind turbines web site," Online: www.energy.siemens.com/hq/en/power-generation/renewables/wind-power/wind-turbines, Accessed 1 Dec. 2011.

[23] Y. Chen, P. Pillay, and A. Khan, "PM wind generator topologies," *IEEE Transactions on Industry Applications*, vol. 41, no. 6, pp. 1619–1626, Nov./Dec. 2005.

[24] A. Aydin, S. Huang, and T. Lipo, "Axial flux permanent magnet disc machines: A review," in *Proc. of the 11th International Power Electronics and Motion Control Conference, EPE-PEMC 2004*, Riga, Latvia, Sep. 2004.

[25] E. Spooner and A. Williamson, "Direct coupled, permanent magnet generators for wind turbine applications," *IEE Proc. Electric Power Applications*, vol. 143, no. 1, pp. 1–8, Jan. 1996.

[26] E. Spooner, P. Gordon, J. Bumby, and C. French, "Lightweight ironless-stator PM generators for direct-drive wind turbines," *IEE Proc. Electric Power Applications*, vol. 152, no. 1, pp. 17–26, Jan. 2005.

[27] T. Tudorache, L. Melcescu, and M. Popescu, "Methods for cogging torque reduction of directly driven PM wind generators," in *Proc. of the 12th International Conference on Optimization of Electrical and Electronic Equipment, OPTIM 2010*, Brasov, Romania, May 2010.

[28] M. Dubois, "Optimized permanent magnet generator topologies for direct-drive wind turbines," Doctoral dissertation, Delft University of Technology, Delft, the Netherlands, 2004.

[29] A. Grauers, "Design of direct-driven permanent-magnet generators for wind turbines," Doctoral dissertation, Chalmers University of Technology, Göteborg, Sweden, 1996.

[30] Y. Zhang and F. Wang, "Choice of pole-slot number combination for PM generator direct-driven by wind turbine," in *Proc. of the Joint International Conference on Power System Technology and IEEE Power India Conference, POWERCON 2008*, New Delhi, India, Oct. 2008.

[31] K.-C. Kim, S.-B. Lim, K.-B. Jang, S.-G. Lee, J. Lee, Y.-G. Son, Y.-K. Yeo, and S.-H. Baek, "Analysis on the direct-driven high power permanent magnet generator for wind turbine," in *Proc. of the 8th International Conference on Electrical Machines and Systems, ICEMS 2005*, Nanjing, China, Sep. 2005.

[32] F. Delfino, G. Denegri, M. Invernizzi, F. Pampararo, R. Procopio, and M. Rossi, "Modeling and control of DDPM wind generators," in *Proc. of the 45th International Universities Power Engineering Conference, UPEC 2010*, Cardiff, UK, Aug./Sep. 2010.

[33] H. Polinder, D. Bang, R. van Rooij, A. McDonald, and M. Mueller, "10 MW wind turbine direct-drive generator design with pitch or active speed stall control," in *Proc. of the IEEE International Electric Machines and Drives Conference, IEMDC 2007*, Antalya, Turkey, May 2007.

[34] J. Pyrhönen, P. Kurronen, and A. Parviainen, "Permanent magnet 3 MW low-speed generator development," in *Proc. of the 17th International Conference on Electrical Machines, ICEM 2006*, Chania, Greece, Sep. 2006.

[35] H. Jussila, "Concentrated winding multiphase permanent magnet machine design and electromagnetic properties - case axial flux machine," Doctoral dissertation, Lappeenranta University of Technology, Lappeenranta, Finland, Dec. 2009, Online: http://urn.fi/URN:ISBN:978-952-214-883-4.

[36] G.-H. Kang, Y.-D. Son, G.-T. Kim, and J. Hur, "A novel cogging torque reduction method for interior-type permanent-magnet motor," *IEEE Transactions on Industry Applications*, vol. 45, no. 1, pp. 161–167, Jan./Feb. 2009.

[37] L. Fang, S.-I. Kim, S.-O. Kwon, and J.-P. Hong, "Novel double-barrier rotor designs in interior-PM motor for reducing torque pulsation," *IEEE Transactions on Magnetics*, vol. 46, no. 6, pp. 2183–2186, Jun. 2010.

[38] J. Kolehmainen and J. Ikäheimo, "Motors with buried magnets for medium-speed applications," *IEEE Transactions on Energy Conversion*, vol. 23, no. 1, pp. 86–91, Mar. 2008.

[39] H.-S. Chen, D. Dorrell, and M.-C. Tsai, "Design and operation of interior permanent-magnet motors with two axial segments and high rotor saliency," *IEEE Transactions on Magnetics*, vol. 46, no. 9, pp. 3664–3675, Sep. 2010.

[40] T. Jahns and W. Soong, "Pulsating torque minimization techniques for permanent magnet AC motor drives-a review," *IEEE Transactions on Industrial Electronics*, vol. 43, no. 2, pp. 321–330, Apr. 1996.

[41] D. Hanselman, "Effect of skew, pole count and slot count on brushless motor radial force, cogging torque and back EMF," *IEE Proc. Electric Power Applications*, vol. 144, no. 5, pp. 325–330, Sep. 1997.

[42] Z. Zhu and D. Howe, "Influence of design parameters on cogging torque in permanent magnet machines," *IEEE Transactions on Energy Conversion*, vol. 15, no. 4, pp. 407–412, Dec. 2000.

[43] S.-M. Hwang, J.-B. Eom, Y.-H. Jung, D.-W. Lee, and B.-S. Kang, "Various design techniques to reduce cogging torque by controlling energy variation in permanent magnet motors," *IEEE Transactions on Magnetics*, vol. 37, no. 4, pp. 2806–2809, Jul. 2001.

[44] N. Bianchi and S. Bolognani, "Design techniques for reducing the cogging torque in surface-mounted PM motors," *IEEE Transactions on Industry Applications*, vol. 38, no. 5, pp. 1259–1265, Sep./Oct. 2002.

[45] M. Łukaniszyn, M. JagieŁa, and R. Wróbel, "Optimization of permanent magnet shape for minimum cogging torque using a genetic algorithm," *IEEE Transactions on Magnetics*, vol. 40, no. 2, pp. 1228–1231, Mar. 2004.

[46] R. Islam, I. Husain, A. Fardoun, and K. McLaughlin, "Permanent-magnet synchronous motor magnet designs with skewing for torque ripple and cogging torque reduction," *IEEE Transactions on Industry Applications*, vol. 45, no. 1, pp. 152–160, Jan./Feb. 2009.

[47] N. Chen, S. Ho, and W. Fu, "Optimization of permanent magnet surface shapes of electric motors for minimization of cogging torque using FEM," *IEEE Transactions on Magnetics*, vol. 46, no. 6, pp. 2478–2481, Jun. 2010.

[48] S. Ho, N. Chen, and W. Fu, "An optimal design method for the minimization of cogging torques of a permanent magnet motor using FEM and genetic algorithm," *IEEE Transactions on Applied Superconductivity*, vol. 20, no. 3, pp. 861–864, Jun. 2010.

[49] D. Wang, X. Wang, Y. Yang, and R. Zhang, "Optimization of magnetic pole shifting to reduce cogging torque in solid-rotor permanent-magnet synchronous motors," *IEEE Transactions on Magnetics*, vol. 46, no. 5, pp. 1228–1234, May 2010.

[50] T. Ishikawa and G. Slemon, "A method of reducing ripple torque in permanent magnet motors without skewing," *IEEE Transactions on Magnetics*, vol. 29, no. 2, pp. 2028–2031, Mar. 1993.

[51] W. Fei and P. Luk, "A new technique of cogging torque suppression in direct-drive permanent-magnet brushless machines," *IEEE Transactions on Industry Applications*, vol. 46, no. 4, pp. 1332–1340, Jul./Aug. 2010.

[52] J. Pyrhönen and The Switch, "Permanent magnet synchronous machine," Canadian Intellectual Property Office (CIPO), Tech. Rep. CA 2331835, May 1999.

[53] F. Caricchi, F. Crescimbini, F. Mezzetti, and E. Santini, "Multistage axial-flux PM machine for wheel direct drive," *IEEE Transactions on Industry Applications*, vol. 32, no. 4, pp. 882–888, Jul./Aug. 1996.

[54] G. Banchieri, "Direct wire cooling in synchronous electrical machines," *United States Patent Office, Pat.No. 3543062*, Nov. 1970.

[55] A. Boglietti, A. Cavagnino, M. Lazzari, and A. Pastorelli, "A simplified thermal model for variable speed self cooled industrial induction motor," in *Proc. of the 37th IEEE Industry Applications Society Annual Meeting, IAS 2002*, Pittsburgh, USA, Oct. 2002.

[56] D. Staton, A. Boglietti, and A. Cavagnino, "Solving the more difficult aspects of electric motor thermal analysis in small and medium size industrial induction motors," *IEEE Transactions on Energy conversion*, vol. 20, no. 3, pp. 620–628, Sep. 2005.

[57] J. Nerg, M. Rilla, and J. Pyrhönen, "Thermal analysis of radial-flux electrical machines with a high power density," *IEEE Transactions on Industrial Electronics*, vol. 55, no. 10, pp. 3543–3554, Oct. 2008.

[58] F. Carter, "Airgap induction," *Electrical World*, vol. 38, no. 22, pp. 884–888, 1901.

[59] R. Richter, *Elektrische Maschinen IV, Die Induktionmaschinen*, 2nd ed. Basel/Stuttgart, Germany: Verlag Birkhäuser, 1954.

[60] D. Lowther and P. Silvester, *Computer-Aided Design in Magnetics*, 1st ed. New York, USA: Springer-Verlag, 1986.

[61] T. Heikkilä, "Permanent magnet synchronous motor for industrial inverter applications - analysis and design," Doctoral dissertation, Lappeenranta University of Technology, Lappeenranta, Finland, Nov. 2002, Online: http://urn.fi/URN:ISBN:952-214-271-9.

[62] B. Cassimere, S. Sudhoff, and D. Sudhoff, "Analytical design model for surface-mounted permanent-magnet synchronous machines," *IEEE Transactions on Energy Conversion*, vol. 24, no. 2, pp. 347–357, Jun. 2009.

[63] P. Viarouge, M. Lajoie-Mazenc, and C. Andrieux, "Design and construction of a brushless permanent magnet servomotor for direct-drive application," *IEEE Transactions on Industry Applications*, vol. IA–23, no. 3, pp. 526–531, May 1987.

[64] Y. Takeda and T. Hirasa, "Current phase control methods for permanent magnet synchronous motors considering saliency," in *Proc. of the 19th Annual IEEE Power Electronics Specialists Conference, PESC 1988*, Kyoto, Japan, Apr. 1988.

[65] S. Morimoto, Y. Takeda, and T. Hirasa, "Current phase control methods for permanent magnet synchronous motors," *IEEE Transactions on Power Electronics*, vol. 5, no. 2, pp. 133–139, Apr. 1990.

[66] S. Morimoto, Y. Tong, Y. Takeda, and T. Hirasa, "Loss minimization control of permanent magnet synchronous motor drives," *IEEE Transactions on Industrial Electronics*, vol. 41, no. 5, pp. 511–517, Oct. 1994.

[67] J. Luukko, "Direct torque control of permanent magnet synchronous machines - analysis and implementation," Doctoral dissertation, Lappeenranta University of Technology, Lappeenranta, Finland, 2000.

[68] T. M. Jahns, G. B. Kliman, and T. W. Neumann, "Interior permanent-magnet synchronous motors for adjustable-speed drives," *IEEE Transactions on Industry Applications*, vol. IA–22, no. 4, pp. 738–747, Jul. 1986.